

Supercurrent Multiplexing with Solid-State Integrated Hybrid Superconducting Electronics

Alessandro Paghi^{1*}, Laura Borgongino¹, Simone Tortorella^{1,2}, Giorgio De Simoni¹, Elia Strambini¹, Lucia Sorba¹, and Francesco Giazotto^{1*}

¹Istituto Nanoscienze-CNR and Scuola Normale Superiore, Piazza San Silvestro 12, 56127 Pisa, Italy.

²Dipartimento di Ingegneria Civile e Industriale, Università di Pisa, Largo Lucio Lazzarino, 56122 Pisa, Italy

*Corresponding authors: alessandro.paghi@nano.cnr.it, francesco.giazotto@sns.it

Keywords: Indium Arsenide (InAs); Josephson Field Effect Transistor (JoFET); Superconducting Switch; Superconducting Multiplexer; Hybrid Superconducting Electronics; III-V Heterostructures.

Abstract

Time Division Multiplexing (TDM) of cryogenic signal lines is a promising technique that can significantly reduce the required space, minimize the cooldown time, and increase the number of measurable quantum devices per cooldown. Here, we report the TDM of supercurrent with a 1-input-8-outputs voltage-actuated hybrid superconducting demultiplexer for the first time. The device comprises 14 ON/OFF InAsOI-based superconducting Josephson Field Effect Transistors (JoFETs) routed with Al traces. Each JoFET features Al as a superconductor and HfO₂ as a gate insulator, and it can entirely suppress the switching current and increase the normal-state resistance by 20 times with a gate voltage of -4.5 V. The superconducting demultiplexer operates up to 100 MHz at 50 mK, features an insertion loss of ~ 0 dB in the superconducting state, and an $\frac{OFF}{ON}$ ratio of ~ 17.5 dB in a 50Ω-matched cryogenic measurement setup. The frequency operation range can be extended by designing the demultiplexer with a proper microwave signal transport layout minimizing, at the same time, the impact of the parasitic electrical elements. These achievements open up the practical implementation of superconducting TDM as a key to drastically reducing I/O lines, costs, and space occupation in a cryostat, enabling the scalability of superconducting electronics.

Introduction

In the past decades, there has been tremendous progress in the experimental development of a quantum computer (QC). This machine would exploit the richness of a quantum wavefunction to run complex algorithms [1][2]. Quantum computing enables unprecedented speedups in solving computational problems, such as drug design [3], novel materials discovery [4], study of molecular dynamics [3][4], machine learning for artificial intelligence [5][6][7], and financial modeling [8]. The internal operation of a QC must be protected from the environment to prevent quantum decoherence and the subsequent degradation of information [1][9][10][11][12][13][14]. For this reason, QCs based on quantum electron states are operated at cryogenic temperatures to preserve quantum coherence, reduce thermal noise, and minimize interactions with the surrounding environment.

In a conventional cryostat, N signal lines come from (to) room temperature electronics and travel to (from) the low-temperature plates connecting to the N ports of the quantum processing unit (QPU) or, more in general, of the device under test (DUT) (Figure 1a). Each signal line significantly impacts the cryostat's costs, space occupied, and temperature stability. Thus, the number of cables is one of the significant constraints in the implementation and scalability of QCs. For example, one of the most advanced QCs, Google Sycamore, uses more than 200 RF coaxial cables to control only 54 qubits [15][16].

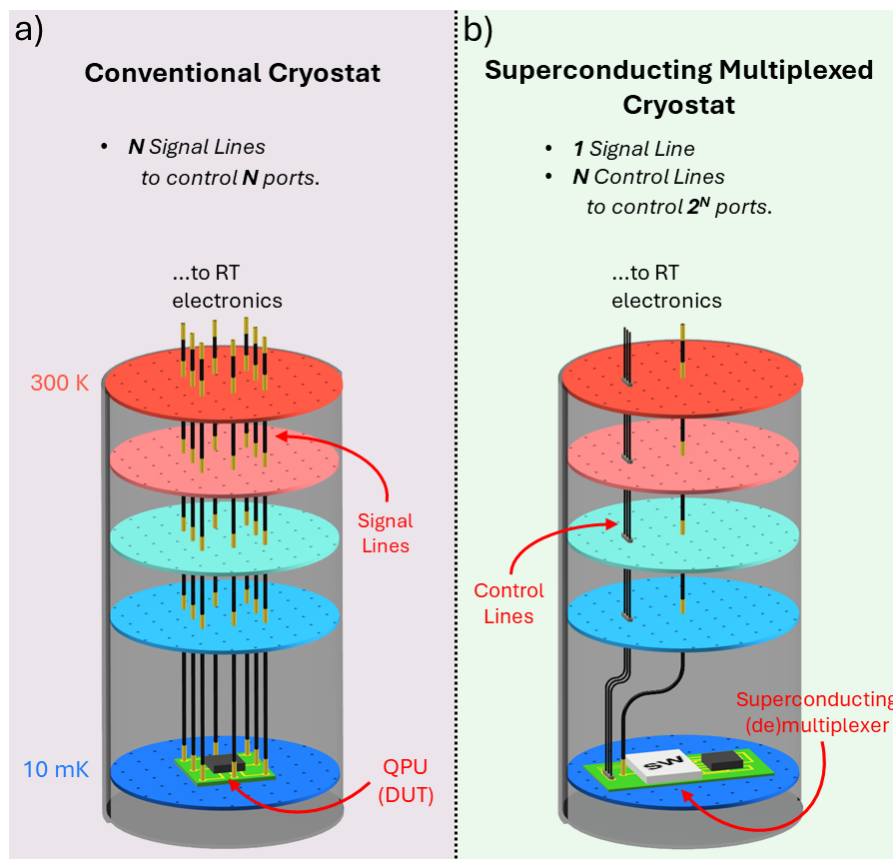


Figure 1: Comparison between conventional and superconducting multiplexed cryostats. a) A conventional cryostat needs N signal lines to control N ports of the QPU. b) A superconducting multiplexed cryostat features N low-frequency high-density control lines and one signal line to control 2^N ports of the QPU. The schematic representations are intended to represent the input or the output lines of the QPU.

To reduce the required space, minimize the cooldown time, and increase the number of measurable devices per cooldown, time division multiplexing (TDM) of RF signal lines is needed to route signals to the QPU. In a multiplexed cryostat, only one signal RF line reaches the lowest temperature plate to connect 2^N ports of the QPU using N control lines (Figure 1b). Nowadays, electromechanical switches are usually involved in TDM of signals at cryogenic temperatures down to a few mK, with the drawbacks of a large amount of volume occupied ($\sim 100 \text{ cm}^3$), reduced I/O lines, and a high switching time ($\sim 10 \text{ ms}$) [17][18][19]. Cryo-CMOS solid-state solutions offer the advantage of a reduced volume together with an increased number of I/O lines and faster-switching events ($\sim 1 \text{ ns}$), allowing at the same time to achieve line-to-line isolations of $30 \div 40 \text{ dBs}$ [20][21][22][23]. On the other hand, static power dissipation accounts for the increase of the temperature of the cold plate of tens of mKs [20][22], while an insertion loss of $1 \div 3 \text{ dBs}$ is usual in the ON-state due to the Ohmic behavior of the chip [22][23]. More importantly, the implementation of TDM with cryo-CMOS platforms is not yet compatible with scalable high-fidelity qubit control due to noticeable thermal radiation emanating from the multiplexer, which requires the signal thermalization between the output of the multiplexer and the quantum chip by a well-thermalized attenuator [22][23]. Along with the previous solutions, more exotic TDM demonstrations are also proposed using platforms based on SiGe-2DEG [24], GaAs-HEMTs [25][26], and InAsNWs [27]. In this context, TDM with a superconducting solid-state multiplexer promises short downtimes between control switching events, near-to-0W static power dissipation, negligible heat injection, and a minimized insertion loss.

Hybrid superconductor-semiconductor architectures enable ideal platforms to develop Josephson Field Effect Transistors (JoFETs) for supercurrent multiplexing [28][29][30][31][32]. The hybrid super-semi JoFET is the key to implement a two-state ON/OFF superconducting/normal building block [33]. The gate tunability of the critical current, as well as the gate tunability of the normal-state resistance, are the fundamental aspects involved in the supercurrent multiplexing operation. In the III-V compound group, InAs is the most common semiconductor employed in the manufacturing of JoFETs thanks to the optimal superconducting proximity effect [28][29][30][34][35][36][37], which provides the electron gas hosted by the InAs layer the ability to support a supercurrent. Among InAs-based platforms, we recently proposed InAs on Insulator (InAsOI) as a new convenient platform to develop planar hybrid superconducting electronics [38][39][40]. Unlike other InAs architectures,

InAsOI features an InAs epilayer grown onto a cryogenic insulating InAlAs metamorphic buffer, which resembles the highly successful silicon-on-insulator (SOI) architecture.

Here, we report for the first time TDM of supercurrent with a 1-input-8-outputs voltage-actuated hybrid superconducting demultiplexer able to reduce the number of input signal lines of a conventional cryostat. As ON-OFF building blocks, we developed InAsOI-based JoFETs featuring Al as superconductor and HfO₂ as gate insulator able to suppress the switching current entirely and to increase the normal-state resistance by 20 times with a gate voltage of -4.5 V. The superconducting demultiplexer operates up to 100 MHz at 50 mK, features an insertion loss of ~ 0 dB in the superconducting state, and an $\frac{OFF}{ON}$ ratio of ~ 17.5 dB in a 50Ω-matched cryogenic measurement setup. The frequency operation range can be extended by designing the demultiplexer with a proper microwave signal transport layout minimizing, at the same time, the impact of the parasitic electrical elements. The reciprocity of the circuit allows, in principle, reversed operations to operate the proposed device as a multiplexer by inverting the I/O ports.

Results and Discussion

The cross-section of a Josephson Field Effect Transistor (JoFET) fabricated on the InAs on Insulator (InAsOI) platform is shown in Figure 2a.

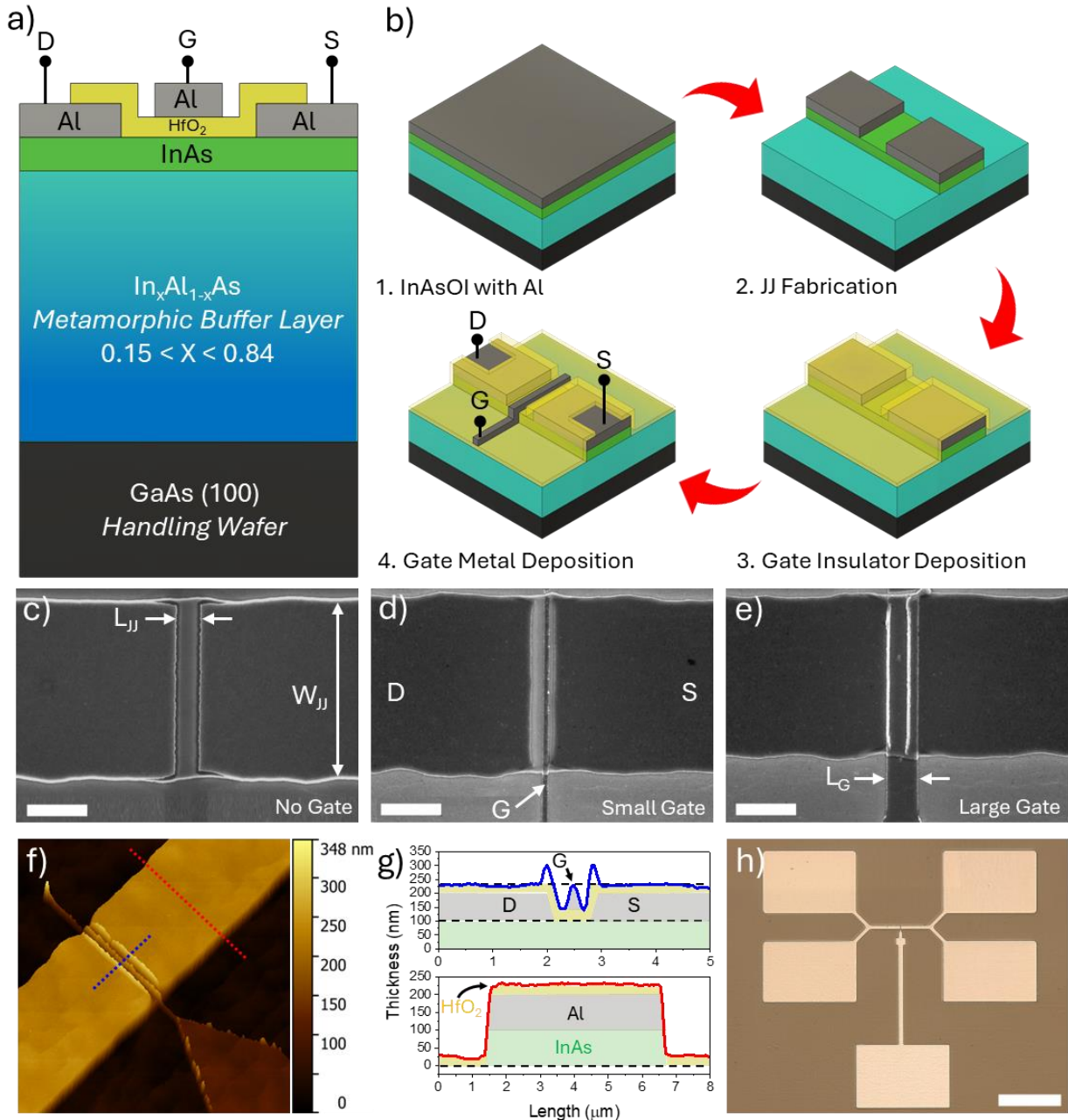


Figure 2: Josephson Field Effect Transistors with InAsOI: concept, manufacturing process, and morphologic characterization. a) Cross-section structure of a JoFET with InAsOI. b) Fabrication process of a JoFET with InAsOI: 1. Superconductive Al deposition onto InAsOI; 2. JJ fabrication via MESA and Al wet etching; 3. Gate insulator deposition via ALD; 4. Gate metal deposition. c,d,e) Top-view SEM images ($10\text{k} \times$) of JoFETs with $W_{JJ} = 6 \mu\text{m}$ and $L_{JJ} = 800 \text{ nm}$ before gate fabrication (c), and after small ($L_G = 200 \text{ nm}$) (d) and large ($L_G = 1000 \text{ nm}$) (d) gate manufacturing; the scalebar is 2 μm . f) xy-plane tilted AFM z-profile of a JoFET featuring $W_{JJ} = 6 \mu\text{m}$, $L_{JJ} = 1200 \text{ nm}$, and $L_G = 100 \text{ nm}$. g) AFM thickness profiles extrapolated from the red and blue dashed line in (f). h) Optical microscope image of the 4-terminal JoFET architecture. The scalebar is 100 μm .

The JoFET is built upon a Molecular Beam Epitaxy (MBE)-grown InAsOI stack consisting, from bottom to top, of a 500- μm -thick semi-insulating GaAs (001) substrate, a $\sim 1.5\text{-}\mu\text{m}$ -thick step-graded $\text{In}_x\text{Al}_{1-x}\text{As}$ metamorphic buffer with X increasing from 0.15 to 0.84, and a 100-nm-thick InAs semiconductive epilayer [38][41]. The InAs layer is n -type doped (extrinsically undoped) due to the InAs natural surface electron accumulation layer [42][43] and deep energy donor levels in the InAlAs band gap [44]. For the InAs epilayer, a sheet electron density (n_{2D}) of $1.35 \times 10^{12} \text{ cm}^{-2}$ and a mobility (μ_n) of $6.7 \times 10^3 \text{ cm}^2/\text{Vs}$ were measured at 3K from Hall measurements. The InAlAs metamorphic buffer behaves as an insulator at cryogenic temperatures [38]. **Figure 2b** depicts the fabrication process of the JoFET. A 100-nm-thick Al layer was deposited onto InAsOI, which acts as the superconductor of the JoFET (**Figure 2b.1**). JoFETs were fabricated via aligned lithographic steps. First, Al and InAs MESA were defined by UV-lithography and manufactured by successive Al and InAs wet etching, setting the Josephson Junction (JJ) width (W_{JJ}) and exposing the InAlAs layer. Then, the JJ length (L_{JJ}) was defined by electron-beam-lithography and Al wet-etching, leaving the underneath InAs unaffected (**Figure 2b.2**). A $\sim 30\text{-nm}$ -thick HfO_2 dielectric layer was conformably deposited via Atomic Layer Deposition (ALD) and used as the gate insulator (**Figure 2b.3**) [45]. The ALD was performed at an optimized temperature of 130°C to preserve the Al/InAs superconducting and transport properties [46]. Eventually, the metal gate was fabricated by electron-beam-lithography and tilted Ti/Al deposition (**Figure 2b.4**), which allowed to conformably cover acute angles left by the InAs wet etching (**Figure S1**). We realized superconductor-semiconductor-superconductor Al-InAs-Al JoFETs with W_{JJ} of 6 μm , L_{JJ} from 500 to 1250 nm, and gate lengths (L_G) from 100 to 1000 nm. **Figures 2c-e** show Scanning Electron Microscopy (SEM) images of JoFETs before and after gate fabrication, from which one can appreciate that the metal gate is aligned and deposited in the middle of the JJ with a precision of $\pm 150 \text{ nm}$, regardless of the gate length. SEM analysis of JoFETs with different values of L_{JJ} and L_G are reported in **Figure S2**. **Figures 2f,g** report the thickness profile of the JoFET surface obtained through Atomic Force Microscopy (AFM) analysis. Finally, an optical microscope photograph of the entire device is shown in **Figure 2h**, from which the 4-terminals architecture of the JoFET, meant for the electrical characterization, can be appreciated.

JoFETs were measured in a dilution fridge equipped with a z-axis superconducting magnet and a DC measurement setup (**Figure S3**); the electrical characterization was performed at 50 mK. **Figure 3a** shows gate-dependent V-I characteristics of a JoFET featuring $W_{JJ} = 6 \mu\text{m}$, $L_{JJ} = 500 \text{ nm}$, and $L_G = 1000 \text{ nm}$. The switching current (I_S) was extracted from the V-I curves as the largest current at 0-voltage drop, while the normal state resistance (R_N) is estimated as the V-I curve slope above I_S .

By decreasing the gate voltage, a reduction of I_S and an increase of R_N is observed. This behavior is confirmed for all the JoFETs tested, regardless of their morphological properties (Figure S4 left column).

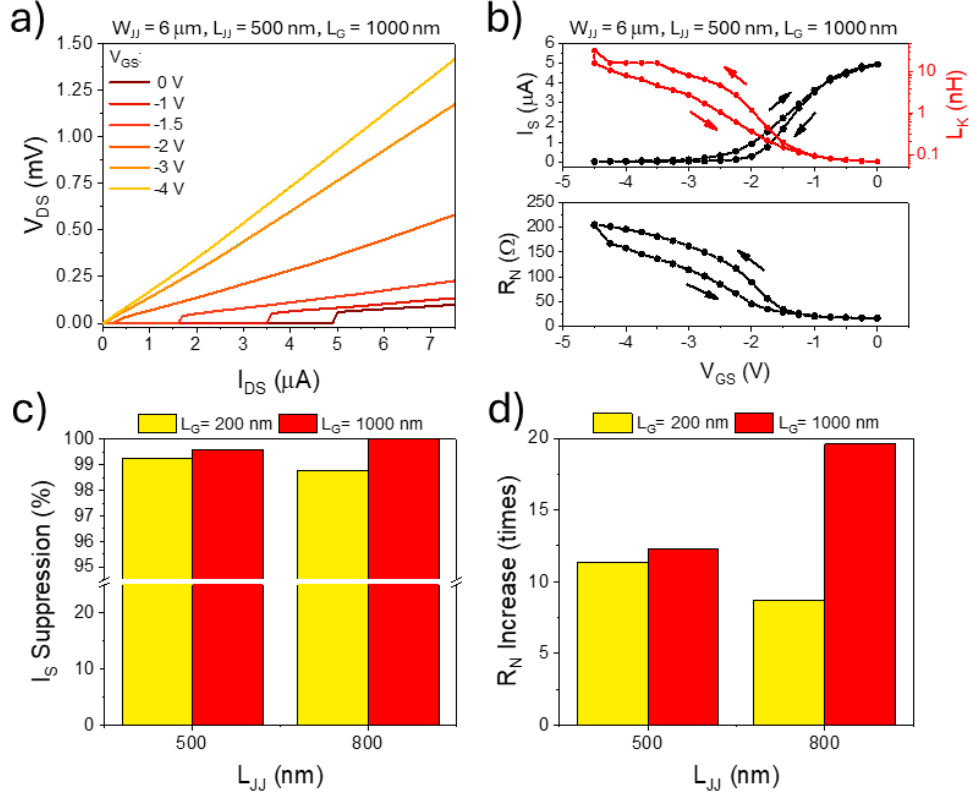


Figure 3: InAsOI-based Josephson Field Effect Transistors electrical characterization. a) Gate-dependent voltage vs. current characteristics of a JoFET featuring $W_{JJ} = 6 \mu\text{m}$, $L_{JJ} = 500 \text{ nm}$, and $L_G = 1000 \text{ nm}$. b) Upward and downward gate-dependent switching current, kinetic inductance, and normal-state resistance of a JoFET featuring $W_{JJ} = 6 \mu\text{m}$, $L_{JJ} = 500 \text{ nm}$, and $L_G = 1000 \text{ nm}$. c,d) Switching current suppression (c) and normal-state resistance increase (d) of JoFET featuring different L_{JJ} and L_G values.

Figure 3b shows the I_S and R_N gate dependence extracted from Figure 3a. Figure 3b top also reports the resulting kinetic inductance ($L_K = \frac{\hbar}{2e \times I_S}$, where \hbar is the reduced Plank's constant and e is the elementary charge). For all the curves, a sigmoidal behavior was observed with the gate voltage, with an evident hysteresis between the upward and downward scans presumably related to electrical traps in the insulator or at the InAs/insulator interface [47][48]. In summary, for all the JoFETs fabricated, the higher the V_{GS} value, the higher the switching current (the lower the normal state resistance), and vice versa (Figure S4 middle column). The zero-voltage and gate-dependent electrical properties of JoFETs rely on the specific transistor morphology. With the increase of L_{JJ} , a reduction of I_S and an increase of R_N is obtained at $V_{GS} = 0 \text{ V}$, as expected (Figure S5). Moreover, at $V_{GS} = 0 \text{ V}$, the larger the gate length, the lower the switching current (the higher the normal state resistance), regardless of

the interelectrode separation (Figure S5). To quantify the ability of the gate to tune the superconducting and transport properties of the JoFETs, we defined the I_S suppression factor, namely $I_{Sup} = 1 - \frac{I_{S@V_{GS}=-4.5V}}{I_{S@V_{GS}=0V}}$ (Figure 3c), and the R_N increase factor, namely $R_{Inc} = \frac{R_{N@V_{GS}=-4.5V}}{R_{N@V_{GS}=0V}}$ (Figure 3d). For both the interelectrode separations tested ($L_{JJ} = 500$ or 800 nm), higher I_{Sup} and R_{Inc} factors were obtained in the case of larger gates compared to the shorter ones, namely $L_G=1000$ nm instead of $L_G=200$ nm. In addition, longer JJs and more extended gates together gave the best I_{Sup} and R_{Inc} . In the case of the JoFET with $L_G=1000$ nm and $L_{JJ}=850$ nm, a 100 % switching current suppression together with ~ 20 times increase of the normal state resistance was obtained, changing the gate voltage in the range from 0 to -4.5 V. Remarkably, a negligible leakage current was collected in the gate voltage operation range (Figure S4 right column). I_{Sup} and R_{Inc} achieved for InAsOI-based JoFETs are on par with the top values obtained in other gate-tunable-critical-current platforms, such as those based on InAs and Ge quantum wells (QWs), InAs and metallic nanowires (NWs), InAs nanosheets (NSs), and graphene (for a comparison see Figure S6 and Table S1). This makes InAsOI a valuable candidate for implementing cryogenic hybrid superconducting electronics, and the InAsOI-based JoFET a promising circuitual element acting as a two-state ON/OFF superconducting/normal building blocks.

We now focus on developing a superconducting 1-input-to-8-outputs (1I8O) analog demultiplexer operating at 50 mK. The roles of the I/O ports can be, in principle, reversed to operate the proposed device as a multiplexer. Figure 4a depicts the schematic diagram of the hierarchical architecture of the demultiplexer, where three signal splitting levels are obtained involving 14 JoFETs (JoFET₀ to JoFET₁₃), one input line (I₀), eight output lines (O₀ to O₇), and six control lines (G₀₀ to G₂₁). Two indexes characterize control lines; the first one, ranging from 0 to 2, refers to the three splitting levels (ranging from left to right in the scheme of Figure 4a), the second identifying the bottom (value of 0) or top (value of 1) output branch of each splitting node. Signal and control lines in the schematic representation are highlighted with red and blue colors, respectively, to improve the readability of the diagram.

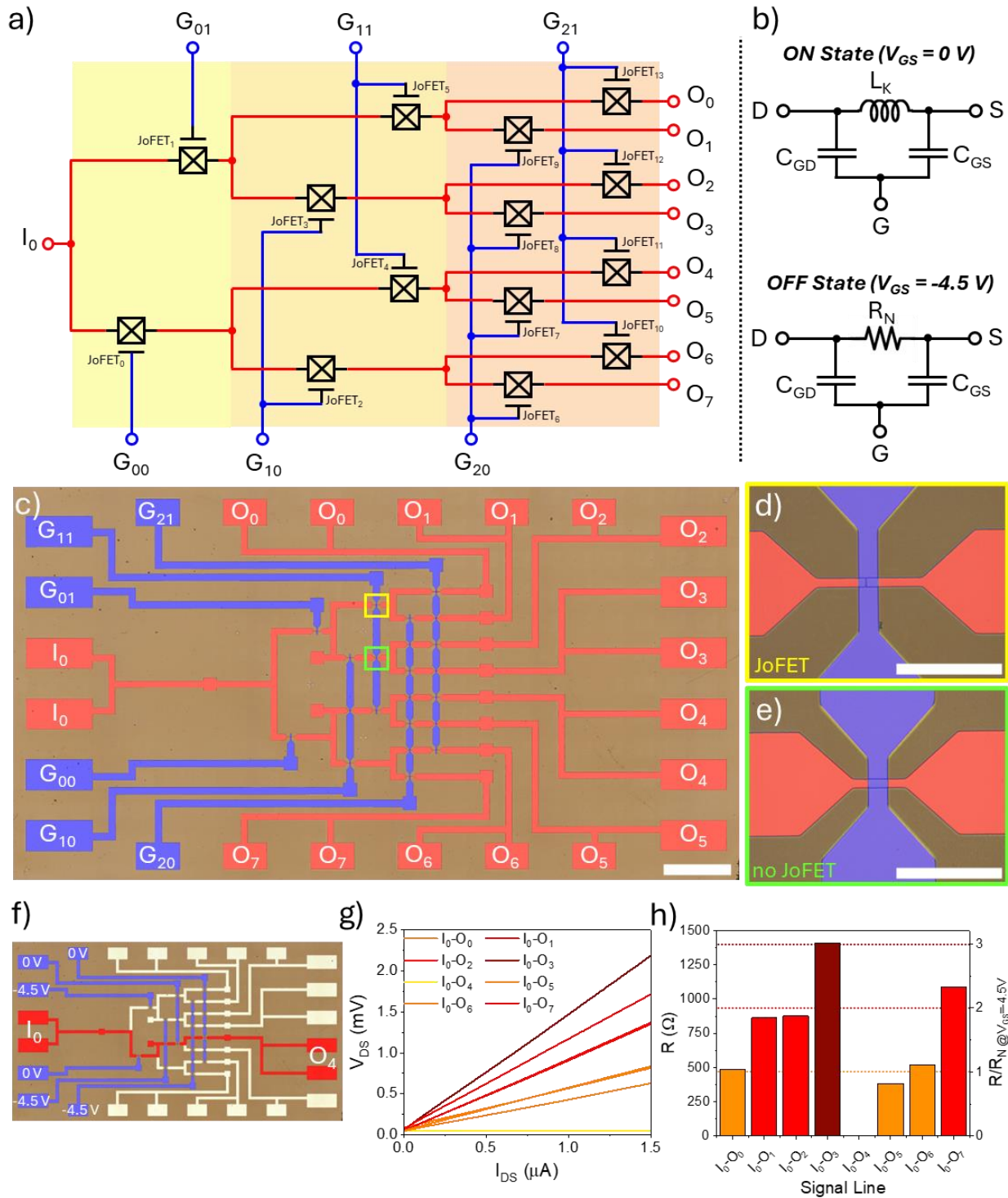


Figure 4: Concept, morphological, and DC electrical characterization of the superconducting 1-input-8-outputs analog demultiplexer. a) Schematic diagram of the superconducting 1I8O demultiplexer. b) Electrical lumped model of the InAsOI-based JoFET. c) False-colors optical microscope image of superconducting 1I8O demultiplexer; the scalebar is $500\ \mu\text{m}$. d,e) False-colors optical microscope image of an overlap between a signal and a gate control line with (d) or without (e) a JoFET; the scalebar is $50\ \mu\text{m}$. f) False-colors optical microscope image of the superconducting 1I8O demultiplexer highlighting the chosen superconducting path and the gate control configuration. g) V-I characteristics of all the 1I8O demultiplexer signal lines with the gate configuration shown in (f). h) Line resistances (left) and normalized line resistances (right) of all the 1I8O demultiplexer signal lines with the gate configuration shown in (f).

The superconducting signal can be hierarchically divided from the input to one of the two following outputs depending on the gate control settings of each signal-splitting node. The number of required JoFETs (U) increases with the number of splitting levels (M) as $U = \sum_{i=1}^M 2^i = \frac{1-2^{M+1}}{-1} - 1$, while the number of output signals (O) increases with the number of control lines (N) as $O = 2^{\frac{N}{2}}$. Remarkably, the number of outputs can be improved to 2^N by using NOT logic ports to invert one of the controls in each signal-splitting level.

Figure 4b depicts the schematic representation of the JoFET in the non-gated superconducting state, i.e., the ON state, and in the gated normal state, i.e., the OFF state. In the ON state ($V_{GS} = 0$ V), the JoFET acts as an inductor with value L_K ; conversely, in the OFF state ($V_{GS} = -4.5$ V), the JoFET works as a resistor with value R_N . The two capacitors between the gate and drain (C_{GD}) and gate and source (C_{GS}) terminals represent the major parasitic elements for both gate settings. The contribution of the JJ capacitance is considered negligible [49]. **Table S2** reports the theoretical frequency-dependent electrical behavior of the fabricated JoFET. The gate-dependent drain-to-source impedance (Z_{DS}) can be changed between the ON state $\frac{1}{Z_{DS_{ON-state}}} = \frac{1}{Z_{L_K}} + \frac{1}{Z_{C_G}}$ (where $Z_{L_K} = j\omega L_K$ is the kinetic inductance impedance, and $Z_{C_G} = \frac{1}{j\omega(C_{GD}+C_{GS})}$ is the gate capacitance impedance), and the OFF state $\frac{1}{Z_{DS_{OFF-state}}} = \frac{1}{R_N} + \frac{1}{Z_{C_G}}$. In both cases, $\omega = 2\pi f$, where f is the operational frequency. Due to its impedance values (see **Table S2**), the fabricated JoFETs can operate in the frequency range from 0 to 300 MHz (DC-VHF radio spectrum).

Figure 4c shows a false-colors optical microscope image of the 1180 demultiplexer fabricated on InAsOI. The chip is 5.5×3 mm² and features two routing levels of 50- μ m-width Al superconducting traces: the underneath for the signal lines (red traces) and the overlying for the gate control lines (blue traces). A HfO₂ layer with 30 nm thickness was used as a gate and metal trace insulator. Each signal line is provided with two pads to perform 4-terminal electrical measurements (**Figure S7**). JoFETs with $W_{JJ} = 4$ μ m, $L_{JJ} = 500$ nm, and $L_G = 9.5$ μ m were fabricated as ON/OFF building blocks. **Figure 4d** shows an overlap between a signal and a gate control line where a JJ is present, i.e., the JoFET. On the other hand, **Figure 4e** exhibits an overlap without active elements, which is used to reach positions on the chip with control lines that cannot be reached without two routing levels.

Table S3 reports the 1180 demultiplexer truth table. For each gate control configuration, only one input-to-output path is fully superconductive, while all the remaining have at least one JoFET in the dissipative state. The signal line resistance is 0 Ω in the case of the non-dissipative path or equal to $1 \times R_N$, $2 \times R_N$, or $3 \times R_N$ according to the number of JoFETs in series in the OFF state along the specific

input-to-output line. As a case of study, we focused on having the I₀-O₄ line superconductive (Figure 4f), with gate control lines set to $V_{G_{00}} = V_{G_{11}} = V_{G_{21}} = 0\text{ V}$ and $V_{G_{01}} = V_{G_{10}} = V_{G_{20}} = -4.5\text{ V}$. Figure S8 depicts the schematic lumped element diagram of the demultiplexer with the applied gate settings to clarify the electrical configuration obtained. Figure 4g shows V-I characteristics of all the 1I8O demultiplexer signal lines. As desired, only I₀-O₄ exhibits a 0 Ω resistance path up to the switching current, while all the other lines present a dissipative path. Line resistances (R) are summarized in Figure 4h, from which we can observe that the $R/R_{N@V_{GS}=-4.5V}$ ratio agrees with what is expected (Table S3). Similar results were also obtained by changing the gating configuration to have I₀-O₆ fully superconductive (Figure S9). This results from the high reproducibility of the electrical properties of both JoFETs and signal lines (Figure S10).

We then evaluated the time-resolved electrical behavior of the superconducting 1I8O demultiplexer. We simultaneously measured signal lines I₀-O₄ and I₀-O₆ while switching between two gating configurations to have only one line in the non-dissipative state at a time. The gate voltages were switched from $V_{G_{10}} = -4.5\text{ V}$ and $V_{G_{11}} = 0\text{ V}$ to cancel the resistance of line I₀-O₄, to $V_{G_{10}} = 0\text{ V}$ and $V_{G_{11}} = -4.5\text{ V}$, to make the path I₀-O₆ superconductive, while leaving all the other gate control lines to $V_{G_{00}} = V_{G_{21}} = 0\text{ V}$ and $V_{G_{01}} = V_{G_{20}} = -4.5\text{ V}$ (see Table S3 and Figure 5a top). The electrical characterization was performed in a dilution fridge equipped with a very-large-frequency (VLF) measurement setup (cut-off frequency $\sim 45\text{ kHz}$) with load resistances (R_L) of $\sim 200\ \Omega$ due to the cryostat wire impedance (Figures S11). The signal-line input current (I_{IN}) is $\sim 1.3\ \mu\text{A}$. The central panel of Figure 5a shows signal line voltages: only one line per time exhibits a zero voltage drop corresponding to the line with all the JoFETs in the ON state. Voltage drops measured for both the lines in the dissipative state are not identical due to the small differences in the gated line resistances (Figures 4h, S10c). Correspondingly, the input current is divided into the two signal lines in agreement with the total line resistance (see Figure 5a bottom). Specifically, the signal line current does not reach 0 A when the line is in the dissipative state due to the cryostat wiring impedance in series to the switch ($R_L \sim 200\ \Omega$). This is a remarkable point to consider when selecting the impedance loads that the superconducting switch can drive.

To complete the electrical characterization of the superconducting 1I8O demultiplexer, we also evaluated the AC electrical performance. We injected into the signal line I₀-O₄ an AC input current with 1 kHz frequency, collecting the voltage drop across the line. Figure 5b shows the time-resolved signal line voltages measured by changing the peak-to-peak value of the input current from 2 μA to 16 μA . When the input current instantaneously overcomes the minimum switching current of the

JoFETs in the $I_0\text{-}O_4$ path (i.e., $I_S = 1.9 \mu\text{A}$ of JoFET₄), a finite voltage drop is detected. The higher the peak-to-peak value of the input current, the higher the signal line voltage drop obtained.

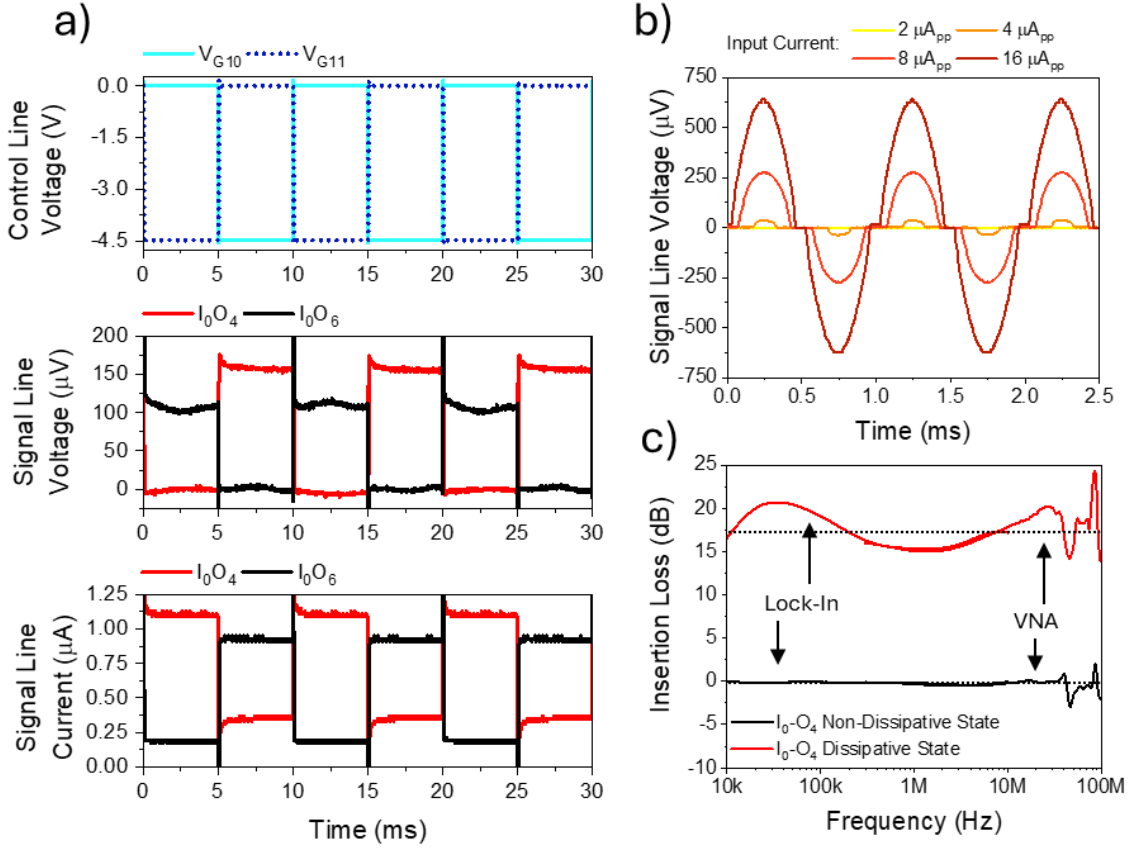


Figure 5: Time-resolved and AC electrical characterization of the superconducting 1-input-8-outputs analog demultiplexer. a) Time-resolved electrical behavior of the superconducting demultiplexer. Time-dependent control line voltages (top), signal line voltages (middle), and signal line currents (bottom). b) Time-resolved $I_0\text{-}O_4$ signal line voltage with different peak-to-peak input currents. c) Frequency-resolved insertion loss of signal line $I_0\text{-}O_4$ in the non-dissipative and dissipative states. Measurements are taken with a lock-in amplifier and a VNA for low and high-frequency ranges, respectively.

By applying an AC signal lower than the minimal critical current supported, we then evaluated the electrical behavior of the superconducting 1I8O demultiplexer in the frequency range from 10 kHz to 100 MHz (LF-VHF radio spectrum) in a dilution fridge equipped with a 50Ω -matched cryogenic measurement setup (maximum operation frequency ~ 300 MHz, [Figures S12](#)). A lock-in amplifier and a vector network analyzer (VNA) were used to measure the magnitude of the forward power gain scattering parameter ($|S_{21}|$) in the 10 kHz - 10 MHz and 300 kHz - 100 MHz ranges, respectively. We simultaneously measured the output powers of signal lines $I_0\text{-}O_4$ and $I_0\text{-}O_6$, injecting an AC input signal with a -80 dBm power level (10 pW, 447 nA_{rms}). Gate settings were chosen to make superconductive only one line at a time. [Figure 5c](#) shows the insertion loss ($IL (dB) = -20\log |S_{21}|$) of the signal line $I_0\text{-}O_4$ in the dissipative and non-dissipative states. When the signal line is superconducting, an insertion loss of ~ 0 dB was measured in the whole frequency range,

demonstrating that the input power is efficiently transferred to the output port of the selected signal line without significant dissipation along the path. This is a remarkable improvement compared to the case in which the demultiplexer in ON-state operates above the critical temperature of Al (specifically at 1.65 K) and, therefore, in a fully dissipative configuration. In this case, the insertion loss increases to ~ 5.5 dB (Figure S13). The latter result highlights the importance of a fully superconducting path between the input and the output port. Compared with conventional gate-tunable cryogenic non-superconducting solutions, it promises a significant competitive advantage of a switchable superconducting system like the one we proposed. On the other hand, when the line is gated in the dissipative state, the insertion loss increases to ~ 17.5 dB, which is relatively constant over all the frequency range tested and allows to achieve an $\frac{OFF}{ON}$ ratio of ~ 17.5 dB. Similar results were also obtained for the signal line I₀-O₆ (Figure S14).

Conclusions

Our work introduces a significant technological advancement in the form of a 1-input-8-outputs voltage-actuated hybrid superconducting demultiplexer. This innovative device is designed to substantially reduce the number of input signal lines required in a conventional cryostat. The key component of this demultiplexer is an InAsOI-based JoFET, which features Al as a superconductor and HfO₂ as a gate insulator. Notably, this JoFET has the capability to completely suppress the switching current and increase the normal-state resistance by 20 times when subjected to a gate voltage of -4.5 V. In this context, the ideal building block should be capable of (i) exhibiting a high switching current in the ON-state, (ii) fully suppressing the switching current in the OFF-state, and (iii) exhibiting a high normal-state resistance in the OFF-state. Thorough testing of the demultiplexer was conducted, pushing its limits up to 100 MHz at 50 mK. The results were remarkable, revealing an insertion loss of approximately 0 dB in the superconducting state and an $\frac{OFF}{ON}$ ratio of approximately 17.5 dB in a 50 Ω -matched cryogenic measurement setup. These findings vividly illustrate the advantage of superconductivity by establishing a lossless path between the input and output ports.

Furthermore, specific strategies to extend the frequency operation range of the demultiplexer have been identified. This includes implementing a meticulous waveguide signal transport layout to minimize power dissipation along the I/O line in the ON-state, as well as addressing the gate capacitance limitation on the OFF-state electrical properties of the JoFET. These pioneering advancements demonstrate the potential for the practical implementation of superconducting TDM, which could lead to a substantial reduction in I/O lines, costs, and space occupation within a cryostat.

Acknowledgments

We thank Stefan Heun for helping to carry out room-temperature and cryogenic measurements to estimate InAs mobility and two-dimensional charge density. This work was supported in part by EU's Horizon 2020 Research and Innovation Framework Program under Grant 964398 (SUPERGATE), by Grant 101057977 (SPECTRUM), and in part by the Piano Nazionale di Ripresa e Resilienza, Ministero dell'Università e della Ricerca (PNRR MUR) Project under Grant PE0000023-NQSTI.

References

- [1] T.D. Ladd, F. Jelezko, R. Laflamme, Y. Nakamura, C. Monroe, J.L. O'Brien, Quantum computers, *Nature*. 464 (2010) 45–53. <https://doi.org/10.1038/nature08812>.
- [2] M. Brooks, Quantum computers: what are they good for?, *Nature*. 617 (2023) S1–S3. <https://doi.org/10.1038/d41586-023-01692-9>.
- [3] P.J. Ollitrault, G. Mazzola, I. Tavernelli, Nonadiabatic Molecular Quantum Dynamics with Quantum Computers, *Phys. Rev. Lett.* 125 (2020) 260511. <https://doi.org/10.1103/PhysRevLett.125.260511>.
- [4] P.J. Ollitrault, A. Miessen, I. Tavernelli, Molecular Quantum Dynamics: A Quantum Computing Perspective, *Acc. Chem. Res.* 54 (2021) 4229–4238. <https://doi.org/10.1021/acs.accounts.1c00514>.
- [5] H.-Y. Huang, M. Broughton, J. Cotler, S. Chen, J. Li, M. Mohseni, H. Neven, R. Babbush, R. Kueng, J. Preskill, J.R. McClean, Quantum advantage in learning from experiments, *Science* (80-.). 376 (2022) 1182–1186. <https://doi.org/10.1126/science.abn7293>.
- [6] S.B. Ramezani, A. Sommers, H.K. Manchukonda, S. Rahimi, A. Amirlatifi, Machine Learning Algorithms in Quantum Computing: A Survey, in: 2020 Int. Jt. Conf. Neural Networks, IEEE, 2020: pp. 1–8. <https://doi.org/10.1109/IJCNN48605.2020.9207714>.
- [7] M. Schuld, I. Sinayskiy, F. Petruccione, An introduction to quantum machine learning, *Contemp. Phys.* 56 (2015) 172–185. <https://doi.org/10.1080/00107514.2014.964942>.
- [8] D. Herman, C. Googin, X. Liu, Y. Sun, A. Galda, I. Safro, M. Pistoia, Y. Alexeev, Quantum computing for finance, *Nat. Rev. Phys.* 5 (2023) 450–465. <https://doi.org/10.1038/s42254-023-00603-1>.
- [9] J.M. Zadrozny, J. Niklas, O.G. Poluektov, D.E. Freedman, Millisecond coherence time in a tunable molecular electronic spin qubit, *ACS Cent. Sci.* 1 (2015) 488–492. <https://doi.org/10.1021/acscentsci.5b00338>.
- [10] Y. Wang, M. Um, J. Zhang, S. An, M. Lyu, J.-N. Zhang, L.-M. Duan, D. Yum, K. Kim, Single-qubit quantum memory exceeding ten-minute coherence time, *Nat. Photonics.* 11 (2017) 646–650. <https://doi.org/10.1038/s41566-017-0007-1>.
- [11] P. Wang, C.-Y. Luan, M. Qiao, M. Um, J. Zhang, Y. Wang, X. Yuan, M. Gu, J. Zhang, K. Kim, Single ion qubit with estimated coherence time exceeding one hour, *Nat. Commun.* 12 (2021) 233. <https://doi.org/10.1038/s41467-020-20330-w>.
- [12] A.P.M. Place, L.V.H. Rodgers, P. Mundada, B.M. Smitham, M. Fitzpatrick, Z. Leng, A. Premkumar, J. Bryon, A. Vrajitoarea, S. Sussman, G. Cheng, T. Madhavan, H.K. Babla, X.H. Le, Y. Gang, B. Jäck, A. Gyenis, N. Yao, R.J. Cava, N.P. de Leon, A.A. Houck, New material platform for superconducting transmon qubits with coherence times exceeding 0.3 milliseconds, *Nat. Commun.* 12 (2021) 1779. <https://doi.org/10.1038/s41467-021-22030-5>.
- [13] A. Somoroff, Q. Ficheux, R.A. Mencia, H. Xiong, R. Kuzmin, V.E. Manucharyan, Millisecond Coherence in a Superconducting Qubit, *Phys. Rev. Lett.* 130 (2023) 267001. <https://doi.org/10.1103/PhysRevLett.130.267001>.
- [14] X. Zhou, X. Li, Q. Chen, G. Koolstra, G. Yang, B. Dizdar, Y. Huang, C.S. Wang, X. Han, X.

- Zhang, D.I. Schuster, D. Jin, Electron charge qubit with 0.1 millisecond coherence time, *Nat. Phys.* 20 (2024) 116–122. <https://doi.org/10.1038/s41567-023-02247-5>.
- [15] F. Arute, K. Arya, R. Babbush, D. Bacon, J.C. Bardin, R. Barends, R. Biswas, S. Boixo, F.G.S.L. Brandao, D.A. Buell, B. Burkett, Y. Chen, Z. Chen, B. Chiaro, R. Collins, W. Courtney, A. Dunsworth, E. Farhi, B. Foxen, A. Fowler, C. Gidney, M. Giustina, R. Graff, K. Guerin, S. Habegger, M.P. Harrigan, M.J. Hartmann, A. Ho, M. Hoffmann, T. Huang, T.S. Humble, S. V. Isakov, E. Jeffrey, Z. Jiang, D. Kafri, K. Kechedzhi, J. Kelly, P. V. Klimov, S. Knysh, A. Korotkov, F. Kostritsa, D. Landhuis, M. Lindmark, E. Lucero, D. Lyakh, S. Mandrà, J.R. McClean, M. McEwen, A. Megrant, X. Mi, K. Michielsen, M. Mohseni, J. Mutus, O. Naaman, M. Neeley, C. Neill, M.Y. Niu, E. Ostby, A. Petukhov, J.C. Platt, C. Quintana, E.G. Rieffel, P. Roushan, N.C. Rubin, D. Sank, K.J. Satzinger, V. Smelyanskiy, K.J. Sung, M.D. Trevithick, A. Vainsencher, B. Villalonga, T. White, Z.J. Yao, P. Yeh, A. Zalcman, H. Neven, J.M. Martinis, Quantum supremacy using a programmable superconducting processor, *Nature*. 574 (2019) 505–510. <https://doi.org/10.1038/s41586-019-1666-5>.
- [16] F. Arute, K. Arya, R. Babbush, D. Bacon, J.C. Bardin, R. Barends, S. Boixo, M. Broughton, B.B. Buckley, D.A. Buell, B. Burkett, N. Bushnell, Y. Chen, Z. Chen, B. Chiaro, R. Collins, W. Courtney, S. Demura, A. Dunsworth, E. Farhi, A. Fowler, B. Foxen, C. Gidney, M. Giustina, R. Graff, S. Habegger, M.P. Harrigan, A. Ho, S. Hong, T. Huang, W.J. Huggins, L. Ioffe, S. V. Isakov, E. Jeffrey, Z. Jiang, C. Jones, D. Kafri, K. Kechedzhi, J. Kelly, S. Kim, P. V. Klimov, A. Korotkov, F. Kostritsa, D. Landhuis, P. Laptev, M. Lindmark, E. Lucero, O. Martin, J.M. Martinis, J.R. McClean, M. McEwen, A. Megrant, X. Mi, M. Mohseni, W. Mroczkiewicz, J. Mutus, O. Naaman, M. Neeley, C. Neill, H. Neven, M.Y. Niu, T.E. O’Brien, E. Ostby, A. Petukhov, H. Putterman, C. Quintana, P. Roushan, N.C. Rubin, D. Sank, K.J. Satzinger, V. Smelyanskiy, D. Strain, K.J. Sung, M. Szalay, T.Y. Takeshita, A. Vainsencher, T. White, N. Wiebe, Z.J. Yao, P. Yeh, A. Zalcman, Hartree-Fock on a superconducting qubit quantum computer, *Science* (80-.). 369 (2020) 1084–1089. <https://doi.org/10.1126/science.abb9811>.
- [17] J.-H. Yeh, S.M. Anlage, In situ broadband cryogenic calibration for two-port superconducting microwave resonators, *Rev. Sci. Instrum.* 84 (2013). <https://doi.org/10.1063/1.4797461>.
- [18] D.E. Oates, R.L. Slattery, D.J. Hover, Cryogenic test fixture for two-port calibration at 4.2 K and above, in: 2017 89th ARFTG Microw. Meas. Conf., IEEE, 2017: pp. 1–4. <https://doi.org/10.1109/ARFTG.2017.8000842>.
- [19] S.-H. Shin, M. Stanley, J. Skinner, S.E. de Graaf, N.M. Ridler, Broadband Coaxial S-Parameter Measurements for Cryogenic Quantum Technologies, *IEEE Trans. Microw. Theory Tech.* 72 (2024) 2193–2201. <https://doi.org/10.1109/TMTT.2023.3322909>.
- [20] B. Paquelet Wuetz, P.L. Bavdaz, L.A. Yeoh, R. Schouten, H. van der Does, M. Tiggelman, D. Sabbagh, A. Sammak, C.G. Almudever, F. Sebastiano, J.S. Clarke, M. Veldhorst, G. Scappucci, Multiplexed quantum transport using commercial off-the-shelf CMOS at subkelvin temperatures, *Npj Quantum Inf.* 6 (2020) 43. <https://doi.org/10.1038/s41534-020-0274-4>.
- [21] A. Ruffino, T.-Y. Yang, J. Michniewicz, Y. Peng, E. Charbon, M.F. Gonzalez-Zalba, A cryo-CMOS chip that integrates silicon quantum dots and multiplexed dispersive readout electronics, *Nat. Electron.* 5 (2021) 53–59. <https://doi.org/10.1038/s41928-021-00687-6>.
- [22] A. Potočník, S. Brebels, J. Verjauw, R. Acharya, A. Grill, D. Wan, M. Mongillo, R. Li, T. Ivanov, S. Van Winckel, F.A. Mohiyaddin, B. Govoreanu, J. Craninckx, I.P. Radu, Millikelvin temperature cryo-CMOS multiplexer for scalable quantum device characterisation, *Quantum Sci. Technol.* 7 (2022) 015004. <https://doi.org/10.1088/2058-9565/ac29a1>.
- [23] R. Acharya, S. Brebels, A. Grill, J. Verjauw, T. Ivanov, D.P. Lozano, D. Wan, J. Van

- Damme, A.M. Vadiraj, M. Mongillo, B. Govoreanu, J. Craninckx, I.P. Radu, K. De Greve, G. Gielen, F. Catthoor, A. Potočnik, Multiplexed superconducting qubit control at millikelvin temperatures with a low-power cryo-CMOS multiplexer, *Nat. Electron.* 6 (2023) 900–909. <https://doi.org/10.1038/s41928-023-01033-8>.
- [24] D.R. Ward, D.E. Savage, M.G. Lagally, S.N. Coppersmith, M.A. Eriksson, Integration of on-chip field-effect transistor switches with dopantless Si/SiGe quantum dots for high-throughput testing, *Appl. Phys. Lett.* 102 (2013). <https://doi.org/10.1063/1.4807768>.
- [25] H. Al-Taie, L.W. Smith, B. Xu, P. See, J.P. Griffiths, H.E. Beere, G.A.C. Jones, D.A. Ritchie, M.J. Kelly, C.G. Smith, Cryogenic on-chip multiplexer for the study of quantum transport in 256 split-gate devices, *Appl. Phys. Lett.* 102 (2013). <https://doi.org/10.1063/1.4811376>.
- [26] J.M. Hornibrook, J.I. Colless, I.D. Conway Lamb, S.J. Pauka, H. Lu, A.C. Gossard, J.D. Watson, G.C. Gardner, S. Fallahi, M.J. Manfra, D.J. Reilly, Cryogenic Control Architecture for Large-Scale Quantum Computing, *Phys. Rev. Appl.* 3 (2015) 024010. <https://doi.org/10.1103/PhysRevApplied.3.024010>.
- [27] D. Olšteins, G. Nagda, D.J. Carrad, D. V. Beznasyuk, C.E.N. Petersen, S. Martí-Sánchez, J. Arbiol, T.S. Jespersen, Cryogenic multiplexing using selective area grown nanowires, *Nat. Commun.* 14 (2023) 7738. <https://doi.org/10.1038/s41467-023-43551-1>.
- [28] T. Akazaki, H. Takayanagi, J. Nitta, T. Enoki, A Josephson field effect transistor using an InAs-inserted-channel In_{0.52}Al_{0.48}As/In_{0.53}Ga_{0.47}As inverted modulation-doped structure, *Appl. Phys. Lett.* 68 (1996) 418–420. <https://doi.org/10.1063/1.116704>.
- [29] J. Shabani, M. Kjaergaard, H.J. Suominen, Y. Kim, F. Nichele, K. Pakrouski, T. Stankevic, R.M. Lutchyn, P. Krogstrup, R. Feidenhans'l, S. Kraemer, C. Nayak, M. Troyer, C.M. Marcus, C.J. Palmstrøm, Two-dimensional epitaxial superconductor-semiconductor heterostructures: A platform for topological superconducting networks, *Phys. Rev. B.* 93 (2016) 155402. <https://doi.org/10.1103/PhysRevB.93.155402>.
- [30] Y.-J. Doh, J.A. van Dam, A.L. Roest, E.P.A.M. Bakkers, L.P. Kouwenhoven, S. De Franceschi, Tunable Supercurrent Through Semiconductor Nanowires, *Science* (80-.). 309 (2005) 272–275. <https://doi.org/10.1126/science.1113523>.
- [31] F. Vigneau, R. Mizokuchi, D.C. Zanuz, X. Huang, S. Tan, R. Maurand, S. Frolov, A. Sammak, G. Scappucci, F. Lefloch, S. De Franceschi, Germanium Quantum-Well Josephson Field-Effect Transistors and Interferometers, *Nano Lett.* 19 (2019) 1023–1027. <https://doi.org/10.1021/acs.nanolett.8b04275>.
- [32] A.A. Generalov, K.L. Viisanen, J. Senior, B.R. Ferreira, J. Ma, M. Möttönen, M. Prunnila, H. Bohuslavskyi, Wafer-scale CMOS-compatible graphene Josephson field-effect transistors, *Appl. Phys. Lett.* 125 (2024). <https://doi.org/10.1063/5.0203515>.
- [33] T.D. Clark, R.J. Prance, A.D.C. Grassie, Feasibility of hybrid Josephson field effect transistors, *J. Appl. Phys.* 51 (1980) 2736–2743. <https://doi.org/10.1063/1.327935>.
- [34] M. Amado, A. Fornieri, G. Biasiol, L. Sorba, F. Giazotto, A ballistic two-dimensional-electron-gas Andreev interferometer, *Appl. Phys. Lett.* 104 (2014) 1–5. <https://doi.org/10.1063/1.4884952>.
- [35] A. Fornieri, M. Amado, F. Carillo, F. Dolcini, G. Biasiol, L. Sorba, V. Pellegrini, F. Giazotto, A ballistic quantum ring Josephson interferometer, *Nanotechnology.* 24 (2013) 245201. <https://doi.org/10.1088/0957-4484/24/24/245201>.
- [36] M. Amado, A. Fornieri, F. Carillo, G. Biasiol, L. Sorba, V. Pellegrini, F. Giazotto, Electrostatic tailoring of magnetic interference in quantum point contact ballistic Josephson junctions, *Phys. Rev. B.* 87 (2013) 134506. <https://doi.org/10.1103/PhysRevB.87.134506>.
- [37] S. Roddaro, A. Pescaglioni, D. Ercolani, L. Sorba, F. Giazotto, F. Beltram, Hot-electron effects in InAs nanowire Josephson junctions, *Nano Res.* 4 (2011) 259–265. <https://doi.org/10.1007/s12274-010-0077-6>.
- [38] A. Paghi, G. Trupiano, G. De Simoni, O. Arif, L. Sorba, F. Giazotto, InAs on Insulator: A

New Platform for Cryogenic Hybrid Superconducting Electronics, ArXiv. (2024).
<http://arxiv.org/abs/2405.07630>.

- [39] F. Giazotto, G. De Simoni, L. Sorba, A. Paghi, O. Arif, C. Puglia, Giunzione Josephson e Transistor Superconduttivo ad Effetto di Campo, Filling Number: 102024000008983, 2024.
- [40] S. Battisti, G. De Simoni, A. Braggio, A. Paghi, L. Sorba, F. Giazotto, Extremely weak subkelvin electron-phonon coupling in InAs On Insulator, ArXiv. (2024).
<http://arxiv.org/abs/2406.15040>.
- [41] O. Arif, L. Canal, E. Ferrari, C. Ferrari, L. Lazzarini, L. Nasi, A. Paghi, S. Heun, L. Sorba, Influence of an Overshoot Layer on the Morphological, Structural, Strain, and Transport Properties of InAs Quantum Wells, *Nanomaterials*. 14 (2024) 592.
<https://doi.org/10.3390/nano14070592>.
- [42] C. Affentauschegg, H.H. Wieder, Properties of InAs/InAlAs heterostructures, *Semicond. Sci. Technol.* 16 (2001) 708–714. <https://doi.org/10.1088/0268-1242/16/8/313>.
- [43] W.M. Strickland, M. Hatefipour, D. Langone, S.M. Farzaneh, J. Shabani, Controlling Fermi level pinning in near-surface InAs quantum wells, *Appl. Phys. Lett.* 121 (2022) 1–6.
<https://doi.org/10.1063/5.0101579>.
- [44] F. Capotondi, G. Biasiol, I. Vobornik, L. Sorba, F. Giazotto, A. Cavallini, B. Fraboni, Two-dimensional electron gas formation in undoped In_{0.75}Ga_{0.25}As/In_{0.75}Al_{0.25}As quantum wells, *J. Vac. Sci. Technol. B Microelectron. Nanom. Struct. Process. Meas. Phenom.* 22 (2004) 702–706. <https://doi.org/10.1116/1.1688345>.
- [45] A. Paghi, S. Battisti, S. Tortorella, G. De Simoni, F. Giazotto, Cryogenic Behavior of High-Permittivity Gate Dielectrics: The Impact of the Atomic Layer Deposition Temperature and the Lithography Patterning Method, ArXiv. (2024). <http://arxiv.org/abs/2407.04501>.
- [46] M. Sütő, T. Prok, P. Makk, M. Kirti, G. Biasiol, S. Csonka, E. Tóvári, Near-surface InAs two-dimensional electron gas on a GaAs substrate: Characterization and superconducting proximity effect, *Phys. Rev. B*. 106 (2022) 235404.
<https://doi.org/10.1103/PhysRevB.106.235404>.
- [47] K. Kukli, J. Aarik, M. Ritala, T. Uustare, T. Sajavaara, J. Lu, J. Sundqvist, A. Aidla, L. Pung, A. Hårsta, M. Leskelä, Effect of selected atomic layer deposition parameters on the structure and dielectric properties of hafnium oxide films, *J. Appl. Phys.* 96 (2004) 5298–5307.
<https://doi.org/10.1063/1.1796513>.
- [48] M. Baik, H.-K. Kang, Y.-S. Kang, K.-S. Jeong, C. Lee, H. Kim, J.-D. Song, M.-H. Cho, Effects of thermal and electrical stress on defect generation in InAs metal–oxide–semiconductor capacitor, *Appl. Surf. Sci.* 467–468 (2019) 1161–1169.
<https://doi.org/10.1016/j.apsusc.2018.10.212>.
- [49] H. Courtois, M. Meschke, J.T. Peltonen, J.P. Pekola, Origin of Hysteresis in a Proximity Josephson Junction, *Phys. Rev. Lett.* 101 (2008) 067002.
<https://doi.org/10.1103/PhysRevLett.101.067002>.

Supporting Information

Supercurrent Multiplexing with Solid-State Integrated Hybrid Superconducting Electronics

Alessandro Paghi^{1*}, Simone Tortorella¹, Laura Borgongino¹, Giorgio De Simoni¹, Elia Strambini¹, Lucia Sorba¹, and Francesco Giazotto^{1*}

¹Istituto Nanoscienze-CNR and Scuola Normale Superiore, Piazza San Silvestro 12, 56127 Pisa, Italy.

²Dipartimento di Ingegneria Civile e Industriale, Università di Pisa, Largo Lucio Lazzarino, 56122 Pisa, Italy

*Corresponding authors: alessandro.paghi@nano.cnr.it, francesco.giazotto@sns.it

Summary

1. Supporting Tables	1
2. Supporting Figures	6
3. Materials and Manufacturing Methods	17
3.1. Materials and Chemicals	17
3.2. InAsOI Heterostructure Growth via Molecular Beam Epitaxy	17
3.3. InAsOI Josephson Field Effect Transistor Fabrication	18
3.4. InAsOI Superconducting 1180 Demultiplexer Fabrication	21
3.5. InAsOI Hall Bars Fabrication	22
3.6. Sample Bonding via Wire Wedge Bonding	23
4. Characterization Methods	23
4.1. Morphological Characterization	23
4.2. Electrical Characterization	24
4.2.1. Cryogenic DC Electrical Characterization of InAsOI Josephson Field Effect Transistors	24
4.2.2. Cryogenic Electrical Characterization of the Superconducting 1180 Demultiplexer	24
4.2.3. Cryogenic and Room Temperature Electrical Characterization of InAsOI	27

1 **1. Supporting Tables**

2 **Table S1. State of the art of JoFETs.** For each platform, the most representative JoFETs are reported. In the case of NWs, “W” stays for the NW
 3 diameter. “*” means that electrical or morphological properties are extrapolated from the figures of the papers and not directly provided by the
 4 authors.

InAsOI															
Specs	Super conductor	L _{JJ} [nm]	W _{JJ} [μm]	I _C (V _{GS} =0V) [μA]	I _C /W _{JJ} (V _{GS} =0V) [μA/μm]	I _C Suppr. [%]	R _N (V _{GS} =0V) [Ω]	R _N Incr. [times]	ΔV _{GS} [V]	Gate Type	Gate Insulator	Gate Distance [nm]	T [mK]	Year	Ref.
$n_{2D}=1.35 \times 10^{12} \text{ cm}^{-2}$, $\mu_n=6700 \text{ cm}^2/\text{Vs}$	Al	800	5	1.14	0.274	100	16.8	19.6	-4.5	Top	HfO ₂	30	50	2024	This Work
$n_{2D}=1.35 \times 10^{12} \text{ cm}^{-2}$, $\mu_n=6700 \text{ cm}^2/\text{Vs}$	Al	500	5	4.92	0.826	99.6	28.7	12.3	-4.5	Top	HfO ₂	30	50	2024	This Work
InAs 3D Substrates															
Specs	Super conductor	L _{JJ} [nm]	W _{JJ} [μm]	I _C (V _{GS} =0V) [μA]	I _C /W _{JJ} (V _{GS} =0V) [μA/μm]	I _C Suppr. [%]	R _N (V _{GS} =0V) [Ω]	R _N Incr. [times]	ΔV _{GS} [V]	Gate Type	Gate Insulator	Gate Distance [nm]	T [mK]	Year	Ref.
<i>p</i> -InAs	Nb	400	-	25	-	99.9	158*	316*	-20	Top	SiO ₂ /Nb _x O _y	100/70	20	1995	[1]
<i>p</i> -InAs	Nb	200	50	75*	1.5*	100*	2*	15*	-20	Top	SiO ₂	-	1800	1999	[2]
InAs 2D QWs															
Specs	Super conductor	L _{JJ} [nm]	W _{JJ} [μm]	I _C (V _{GS} =0V) [μA]	I _C /W _{JJ} (V _{GS} =0V) [μA/μm]	I _C Suppr. [%]	R _N (V _{GS} =0V) [Ω]	R _N Incr. [times]	ΔV _{GS} [V]	Gate Type	Gate Insulator	Gate Distance [nm]	T [mK]	Year	Ref.
Buried-QW t=4 nm, $n_{2D}=1.9 \times 10^{12} \text{ cm}^{-2}$, $\mu_n=155000 \text{ cm}^2/\text{Vs}$	Nb	400	80	20.7	0.259	71*	2.5*	2*	-15	Top	SiO ₂ /InAlAs /InGaAs	100/20 /13.5	1000	1995	[3] [4]
Buried-QW t=4 nm, $n_{2D}=2.3 \times 10^{12} \text{ cm}^{-2}$, $\mu_n=111000 \text{ cm}^2/\text{Vs}$	Nb	350	40	5	0.125	100	16	91250	-1.15	Top	InAlAs /InGaAs	20 /13.5	1000	1995	[5] [6] [7]
Buried-QW $n_{2D}=1.1 \times 10^{12} \text{ cm}^{-2}$, $\mu_n=160000 \text{ cm}^2/\text{Vs}$	Nb	600	20	15.6	0.780	100	5.9	-	-25	Top	SiO ₂	300	1700	2002	[8] [9]
Near-Surface-QW t=7 nm, $\mu_n=17700 \text{ cm}^2/\text{Vs}$	Al	200	3	1.45*	0.483*	100*	90*	10*	-3.5	Top	Al ₂ O ₃	40	30	2016	[10]
Near-Surface-QW t=7 nm, $n_{2D}=1.3 \times 10^{12} \text{ cm}^{-2}$ $\mu_n=15600 \text{ cm}^2/\text{Vs}$	Al	250	3	1.85*	0.616*	100	100*	17*	-2.5	Top	Al ₂ O ₃	40	30	2017	[11]

Near-Surface-QW t=4 nm, $n_{2D}=7.2\times 10^{11}\text{cm}^{-2}$, $\mu_n=14400\text{cm}^2/\text{Vs}$	Al	100	4	4.87*	1.21*	100*	100*	27*	-10	Top	AlO _x	50	20	2019	[12]
Near-Surface-QW t=7 nm, $n_{2D}=8.7\times 10^{11}\text{cm}^{-2}$ $\mu_n=52400\text{cm}^2/\text{Vs}$	Al	40	1.5	1.37*	0.913*	100	270*	4*	-2.2	Top	HfO ₂	30	30	2019	[13]
Buried-QW t=4 nm, $n_{2D}=6.2\times 10^{11}\text{cm}^{-2}$, $\mu_n=160000\text{cm}^2/\text{Vs}$	Nb	900	0.73	-	-	100	-	-	-3	Side	-	1250	350	2019	[14]
Near-Surface-QW t=4 nm, $n_{2D}=3.7\times 10^{11}\text{cm}^{-2}$ $\mu_n=200000\text{cm}^2/\text{Vs}$	Nb	900	3.6	0.095*	0.026*	84*	420*	3.6*	-25	Side	-	-	315	2019	[15]
Near-Surface-QW t=4 nm, $n_{2D}=7\times 10^{11}\text{cm}^{-2}$	Al	100	4	2.25*	0.563*	88*	160*	4*	-2*	Top	h-BN	6	30	2021	[16]
Near-Surface-QW t=7 nm, $n_{2D}=9.6\times 10^{11}\text{cm}^{-2}$ $\mu_n=16800\text{cm}^2/\text{Vs}$	Al	150	4	1.8	0.45	100	323	6*	-8	Top	Al ₂ O ₃	60	30	2021	[17]
Near-Surface-QW t=4 nm, $n_{2D}=3.7\times 10^{12}\text{cm}^{-2}$	Al	250	4	1.9*	0.475*	100*	60*	17.8*	-1.5	Top	Al ₂ O ₃	10	17	2021	[18]
Near-Surface-QW t=4 nm, $n_{2D}=7\times 10^{11}\text{cm}^{-2}$	Al	100	4	4.85*	1.213*	75*	95*	2.7*	-7.5*	Top	AlO _x	50	30	2021	[16]
NW-QW t=30 nm, $\mu_n=3200\text{cm}^2/\text{Vs}$	Al	120	0.18 5	0.048*	0.259*	100	1930*	1.9*	-0.3	Top	HfO ₂	15	20	2021	[19]
Near-Surface-QW t=4 nm, $n_{2D}=4\text{-}6\times 10^{11}\text{cm}^{-2}$ $\mu_n=0.9\text{-}$ $1.3\times 10^2\text{cm}^2/\text{Vs}$	Al	300	9	1.1	0.122	100	34*	48.5*	-3.5	Top	Al ₂ O ₃	50	20	2022	[20]
Near-Surface-QW t=7 nm, $n_{2D}=1.6\times 10^{12}\text{cm}^{-2}$ $\mu_n=12000\text{cm}^2/\text{Vs}$	Al	150	3	0.86*	0.286*	100*	10*	1*	-1	Top	HfO ₂	15	50	2023	[21]
Near-Surface-QW t=8 nm, $n_{2D}=8\times 10^{11}\text{cm}^{-2}$ $\mu_n=18000\text{cm}^2/\text{Vs}$	Al	100	-	0.280	-	100*	80*	9.8*	-0.8	Top	Al ₂ O ₃ /HfO ₂	3/15	10	2024	[22]

InAs 2D NSs															
Specs	Super conductor	L _{JJ} [nm]	W _{JJ} [μm]	I _C (V _{GS} =0V) [μA]	I _C /W _{JJ} (V _{GS} =0V) [μA/μm]	I _C Suppr. [%]	R _N (V _{GS} =0V) [Ω]	R _N Incr. [times]	ΔV _{GS} [V]	Gate Type	Gate Insulator	Gate Distance [nm]	T [mK]	Year	Ref.
t=15-30 nm, n _{2D} =4×10 ¹ cm ⁻² , μ _n =8300cm ² /Vs	Al	90	0.3	0.036*	0.12*	10*	1760*	2.5*	-10	Back	SiO ₂	300	20	2023	[23]
t=15-30 nm, n _{2D} =4×10 ¹ cm ⁻² , μ _n =8300cm ² /Vs	Al	90	0.3	0.067*	0.223*	54*	402*	3*	-8	Top	Al ₂ O ₃	30	20	2023	[23]
InAs 1D NWs															
Specs	Super conductor	L _{JJ} [nm]	W _{JJ} [μm]	I _C (V _{GS} =0V) [μA]	I _C /W _{JJ} (V _{GS} =0V) [μA/μm]	I _C Suppr. [%]	R _N (V _{GS} =0V) [Ω]	R _N Incr. [times]	ΔV _{GS} [V]	Gate Type	Gate Insulator	Gate Distance [nm]	T [mK]	Year	Ref.
n-InAs n _{3D} =2÷10×10 ¹⁸ cm ⁻³ , μ _n =200÷2000cm ² /Vs	Al	100-450	0.04 - 0.13	0.0012	-	100	4500	15.5	-71	Back	SiO ₂	250	40	2005	[24]
n-InAs n _{3D} =1.0×10 ¹⁸ cm ⁻³	Nb	70	0.08	0.0028	0.035	100	3800	2.01*	-20	Back	SiO ₂	-	500	2012	[25]
n-InAs	Nb	55	0.08	0.075	0.938	46.7	1523*	1.56*	-7	Back	-	-	15	2021	[26]
n-InAs	Sn	100	-	0.24*	-	83.7*	962*	5.31*	-0.5	Top	HfO ₂	10	40	2023	[27]
Ge 2D QWs															
Specs	Super conductor	L _{JJ} [nm]	W _{JJ} [μm]	I _C MAX [μA]	I _C /W _{JJ} [μA/μm]	I _C Suppr. [%]	R _N min [Ω]	R _N Incr. [times]	ΔV _{GS} [V]	Gate Type	Gate Insulator	Gate Distance [nm]	T [mK]	Year	Ref.
Near-Surface-QW t=16 nm, p _{2D} =6×10 ¹¹ cm ⁻² , μ _h =500000cm ² /Vs	Al	50	1	0.043 (V _{GS} =-4V)	0.043	100	371* (V _{GS} =-4V)	2.70*	2	Top	Al ₂ O ₃	-	10	2019	[28]
Buried-QW t=16 nm p _{2D} =2÷3×10 ¹¹ cm ⁻² , μ _h ~2÷3×10 ⁵ cm ² /Vs	Al	1000	0.5*	0.006* (V _{GS} =-1.95V)	0.012*	100*	1120* (V _{GS} =-1.95V)	7*	0.95	Top	HfO ₂	40	15	2019	[29]
Buried-QW t=16 nm, p _{2D} =6×10 ¹¹ cm ⁻² , μ _h =5×10 ⁵ cm ² /Vs	Al/Nb	150	-	1 (V _{GS} =-2.5V)	-	94.3*	344* (V _{GS} =-2.5V)	2.90*	1.5	Top	Al ₂ O ₃	20	20	2021	[30]
Graphene															
Specs	Super conductor	L _{JJ} [nm]	W _{JJ} [μm]	I _C [μA]	I _C /W _{JJ} [μA/μm]	I _C Suppr. [%]	R _N [Ω]	R _N Incr. [times]	ΔV _{GS} [V]	Gate Type	Gate Insulator	Gate Distance [nm]	T [mK]	Year	Ref.

Monolayer <i>p</i> -type regime	Nb	150 0	6	1.59* ($V_{GS}=-60$ V)	0.265*	98.7* ($V_{GS}=0$ V)	52* ($V_{GS}=-60$ V)	12.5*	60	Back	SiO ₂	300	300	2018	[31]	
Monolayer <i>n</i> -type regime $\mu_n=300000$ cm ² /Vs	Nb	150 0	6	7 ($V_{GS}=60$ V)	1.167	99.7 ($V_{GS}=0$ V)	19* ($V_{GS}=60$ V)	30*	-60	Back	SiO ₂	300	300	2018	[31]	
Monolayer $p_{2D}=5.5\times 10^{12}$ cm ⁻² $\mu_n=2100$ cm ² /Vs	Nb	250	80	1.9 ($V_{GS}=-50$ V)	0.024	89	40 ($V_{GS}=-50$ V)	4	113.8 5	Back	SiO ₂	300	320	2019	[32]	
Monolayer	Al	300	20	0.9* ($V_{GS}=10$ V)	0.045*	74*	24.1* ($V_{GS}=10$ V)	3.6*	-21.6	Top	Al ₂ O ₃	30	42	2024	[33]	
Monolayer	Al	350	20	1* ($V_{GS}=10$ V)	0.05*	85*	23.8* ($V_{GS}=10$ V)	5.6*	-22.2	Top	Al ₂ O ₃	30	42	2024	[33]	
Monolayer	Al	250	50	2.34* ($V_{GS}=10$ V)	0.047*	80*	14.4* ($V_{GS}=10$ V)	3*	-22.5	Top	Al ₂ O ₃	30	42	2024	[33]	
Monolayer	Al	300	50	3.15* ($V_{GS}=10$ V)	0.063*	77*	13.3* ($V_{GS}=10$ V)	2.1*	-21.1	Top	Al ₂ O ₃	30	42	2024	[33]	
Metal NWs																
Specs	Super conductor	L _{JJ} [nm]	W _{JJ} [μm]	I _c ($V_{GS}=0$ V) [μA]	I _c / W _{JJ} ($V_{GS}=0$ V) [μA/μm]	I _c Suppr. [%]	R _N ($V_{GS}=0$ V) [Ω]	R _N Incr. [times]	ΔV _{GS} [V]	Gate Type	Gate Insulator	Gate Distance [nm]	T [mK]	Year	Ref.	
NW t=30 nm	Ti	900	0.2	11	55	100	45	1	40	Back + Side	-	112*	5	2018	[34]	
NW t = 11 nm	Al	800	0.03	12.3	410	35	320	1	70	Back	-	112*	5	2018	[34]	
DB	Nb	100	0.9	0.03	0.033	90	30	1	40	Side	-	70	30	2020	[35]	
DB t = 60 nm	V	160	0.09	1420	15778	100	110	1	15	Side	-	70	2	2020	[36]	

1

2

3

4 **Table S2. Theoretical frequency dependent electrical behavior of the JoFET in the**
5 **superconducting 1I8O demultiplexer.**

f [Hz]	L_K [pH]	$ Z_{L_K} $ [Ω] <i>ON-state</i>	R_N [Ω] <i>OFF-state</i>	$C_G = C_{GD} + C_{GS}$ [fF]	$ Z_{C_G} $ [Ω]	$ Z_{DS} = Z_{L_K} Z_{C_G}$ [Ω] <i>ON-state</i>	$ Z_{DS} = R_N Z_{C_G}$ [Ω] <i>OFF-state</i>	λ_{GaAs} [mm]
10M	163	0.01	564	169	94175	0.01	560.6	2500
100M	163	0.10	564	169	9417.5	0.1	532.1	250
1G	163	1.02	564	169	941.75	1.0	353.8	25
10G	163	10.2	564	169	94.175	9.2	80.8	2.5

6

7 **Table S3. Superconducting 1I8O demultiplexer truth table.** The highlighted rows are the gate
8 settings studied in the paper.

Gate Control Lines						Line Resistance (Referred To I_0)							
G_{00}	G_{01}	G_{10}	G_{11}	G_{20}	G_{21}	O_0	O_1	O_2	O_3	O_4	O_5	O_6	O_7
-4.5 V	0	-4.5 V	0	-4.5 V	0	0	1R _N	1R _N	2R _N	1R _N	2R _N	2R _N	3R _N
-4.5 V	0	-4.5 V	0	0	-4.5 V	1R _N	0	2R _N	1R _N	2R _N	1R _N	3R _N	2R _N
-4.5 V	0	0	-4.5 V	-4.5 V	0	1R _N	2R _N	0	1R _N	2R _N	3R _N	1R _N	2R _N
-4.5 V	0	0	-4.5 V	0	-4.5 V	2R _N	1R _N	1R _N	0	3R _N	2R _N	2R _N	1R _N
0	-4.5 V	-4.5 V	0	-4.5 V	0	1R _N	2R _N	2R _N	3R _N	0	1R _N	1R _N	2R _N
0	-4.5 V	-4.5 V	0	0	-4.5 V	2R _N	1R _N	3R _N	2R _N	1R _N	0	2R _N	1R _N
0	-4.5 V	0	-4.5 V	-4.5 V	0	2R _N	3R _N	1R _N	2R _N	1R _N	2R _N	0	1R _N
0	-4.5 V	0	-4.5 V	0	-4.5 V	3R _N	2R _N	2R _N	1R _N	2R _N	1R _N	1R _N	0

9

10

11

12

13

14

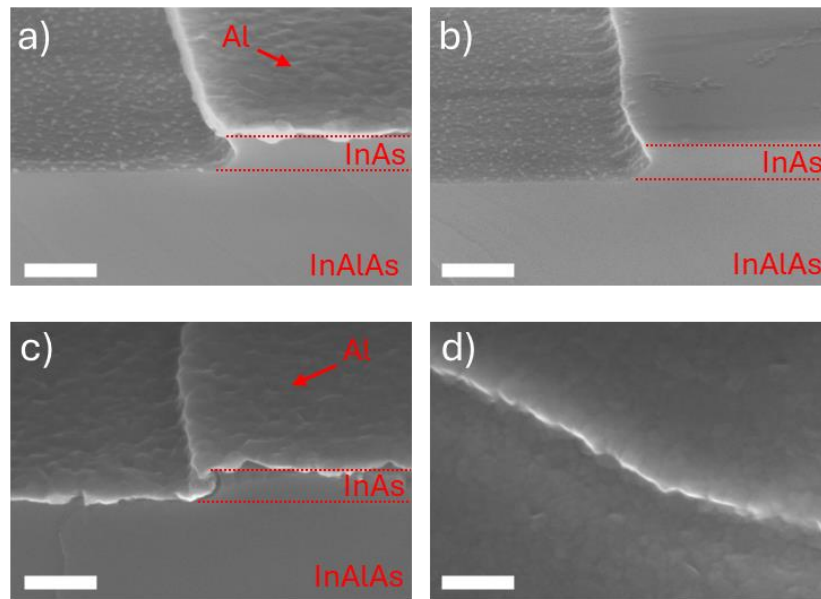
15

16

17

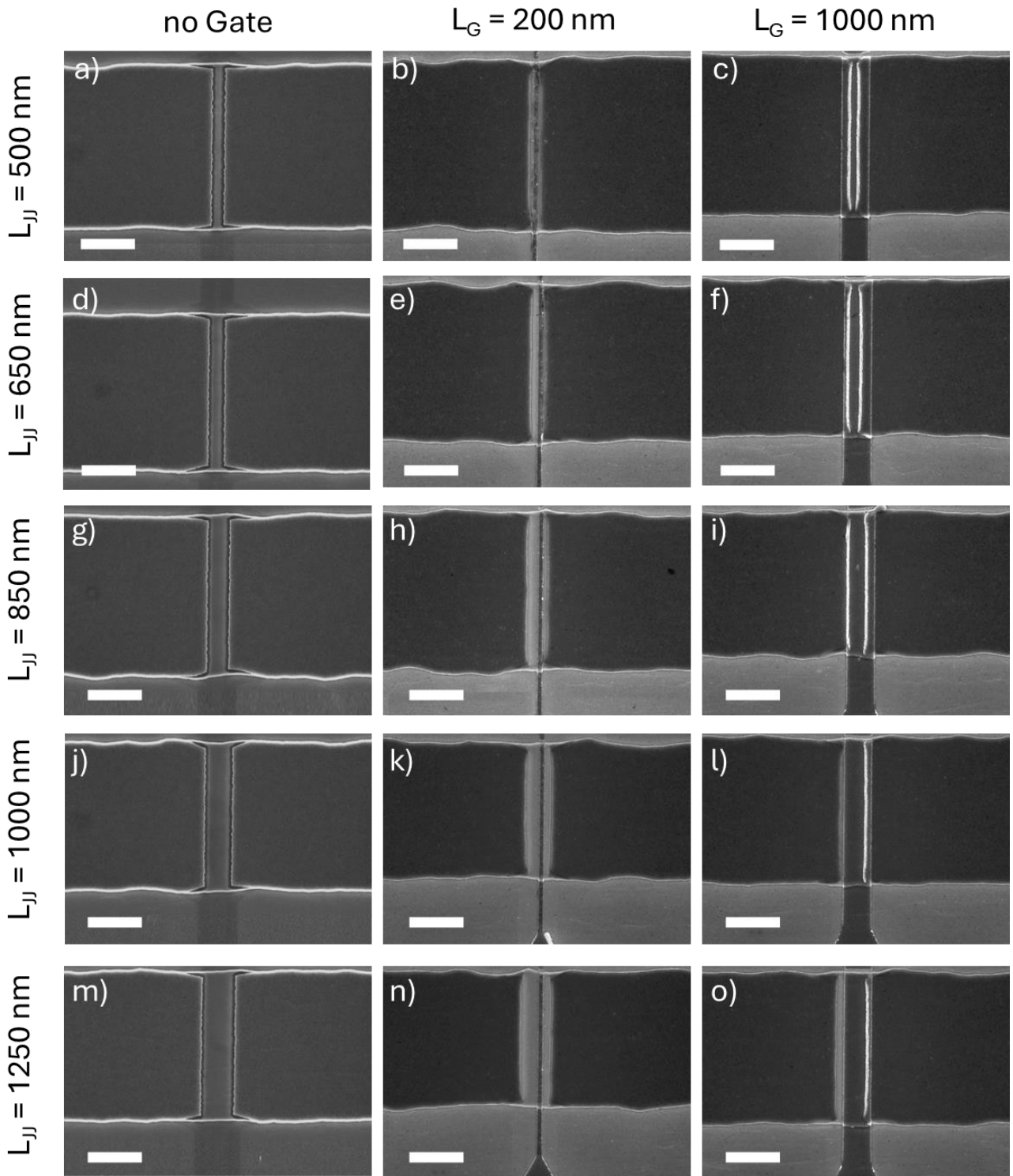
18

19 **2. Supporting Figures**



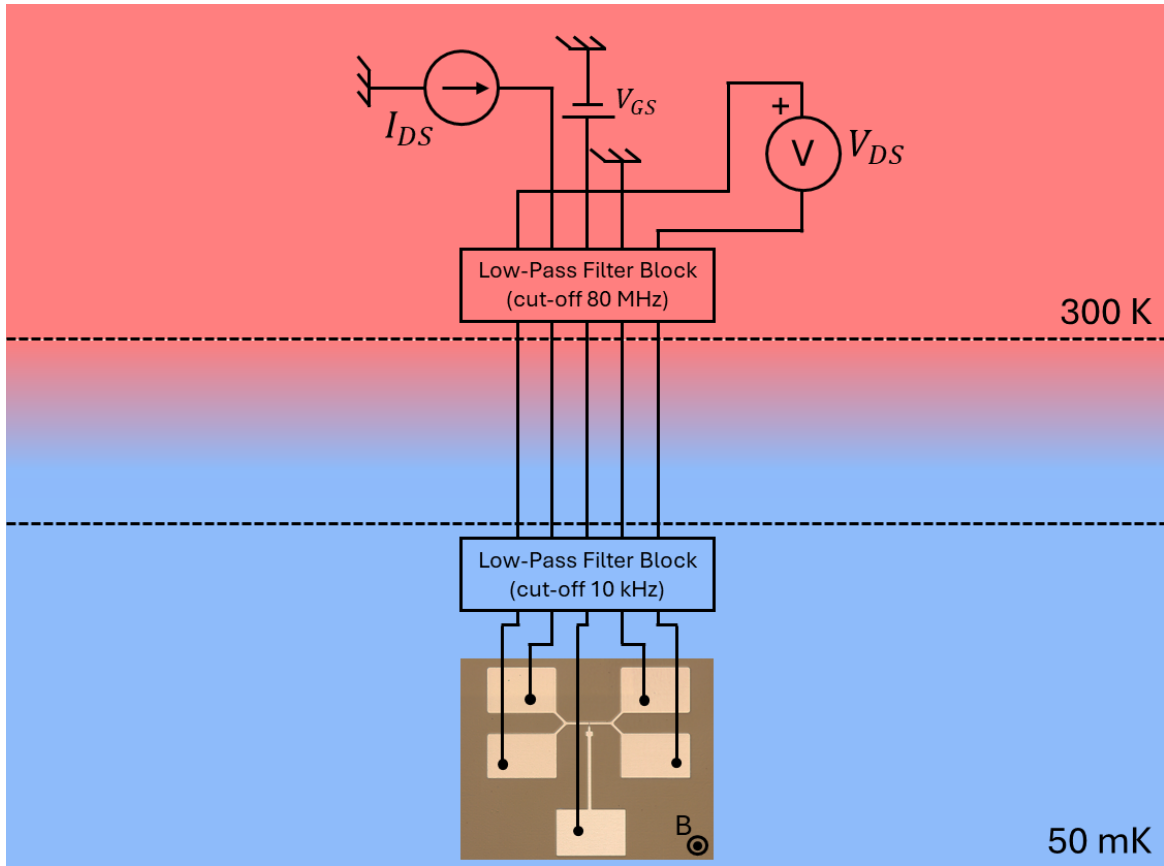
20

21 **Figure S1: Tilted scanning electron microscopy analysis (100k \times) of InAs MESA edge coating**
22 **by metal gate.** (a) InAs profile after MESA definition via wet etching. (b) InAs profile after Al
23 removal from MESA. (c,d) InAs profile coverage via tilted Ti/Al deposition. The scalebar is 200
24 nm.



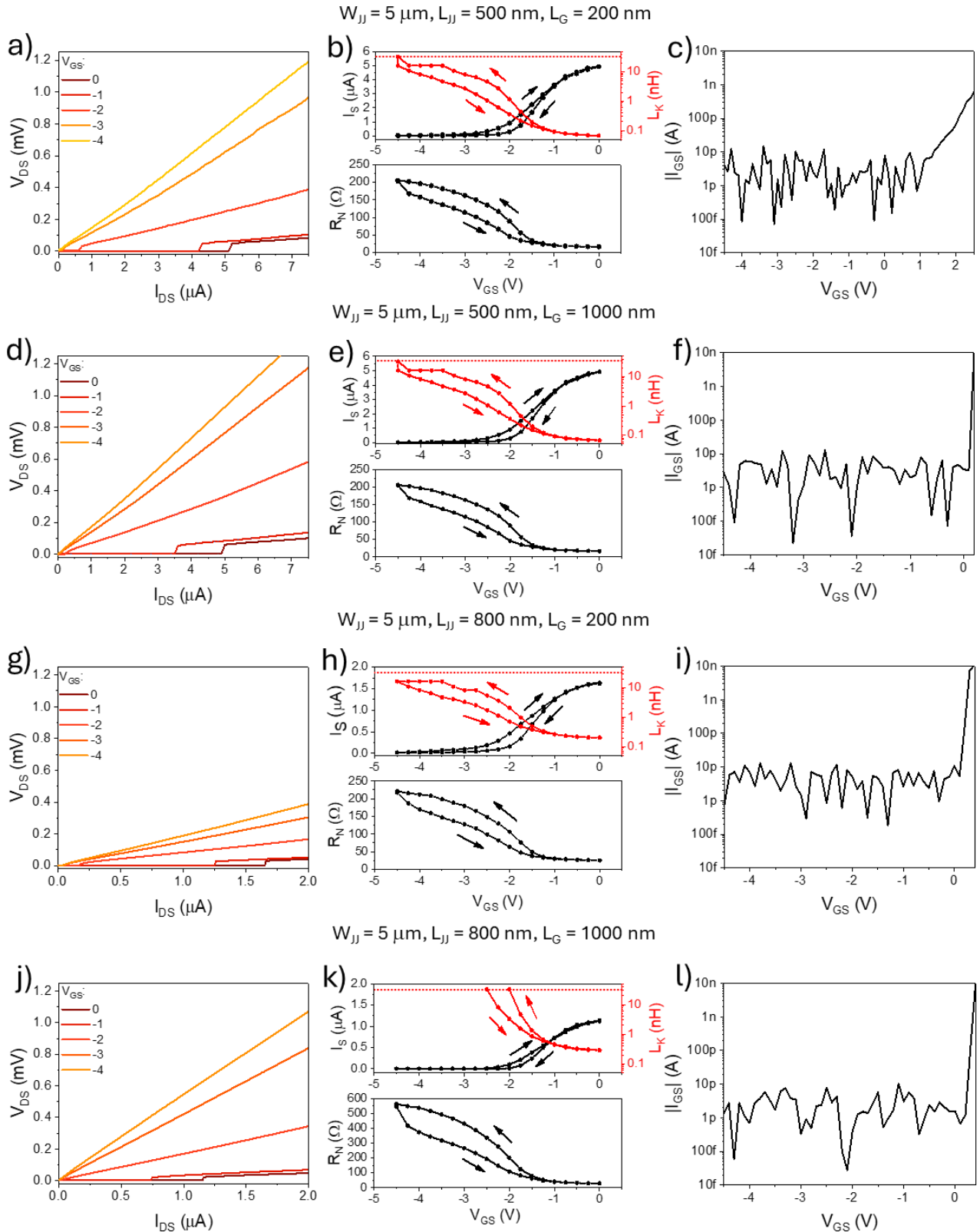
25
26
27
28
29
30
31
32
33
34
35

Figure S2: Top-view scanning electron microscopy analysis (10k \times) of JoFETs. a,d,g,j,m) SEM images of JoFETs before gate architecture manufacturing, i.e., Josephson Junctions, with different interelectrode separations. b,e,h,k,n) SEM images of JoFETs featuring $L_G = 200 \text{ nm}$ with different interelectrode separations. c,f,i,l,o) SEM images of JoFETs featuring $L_G = 1000 \text{ nm}$ with different interelectrode separations. The scalebar is $2 \mu\text{m}$.



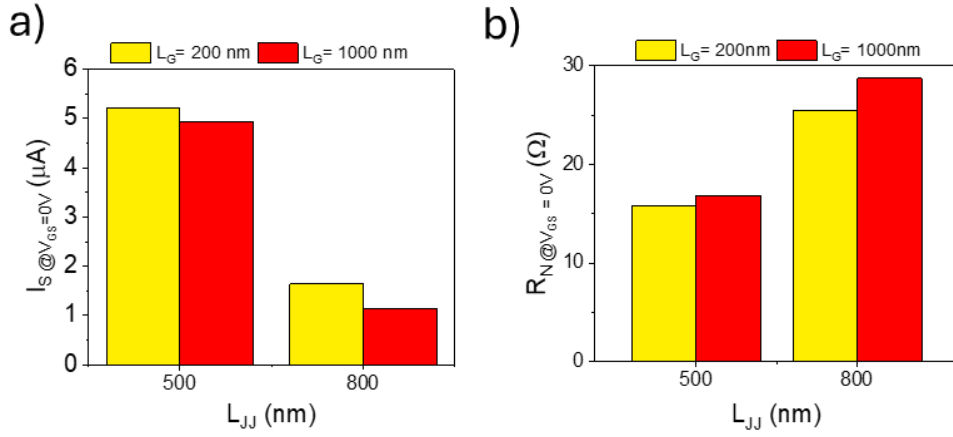
36
37
38

Figure S3: DC measurement setup used to characterize the JoFETs in a dilution fridge equipped with a z-axis superconducting magnet.



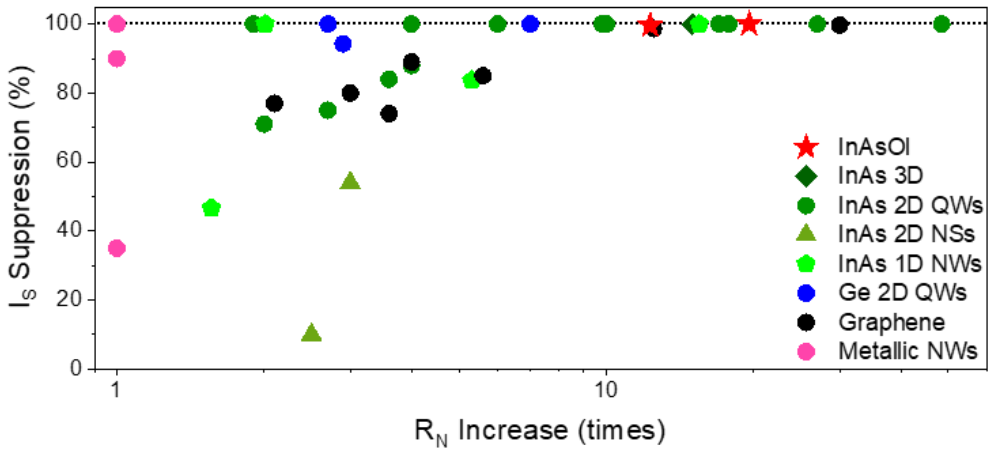
39
 40 **Figure S4: InAsOI-based Josephson Field Effect Transistors electrical characterization.**
 41 a,d,g,j) Gate-dependent voltage vs. current characteristic of JoFETs. b,e,h,k) Upward and
 42 downward gate-dependent switching current, kinetic inductance, and normal state resistance of
 43 JoFETs. c,f,i,l.) Gate leakage current vs. gate voltage of JoFETs. Measurements were performed at
 44 50 mK.
 45
 46

47



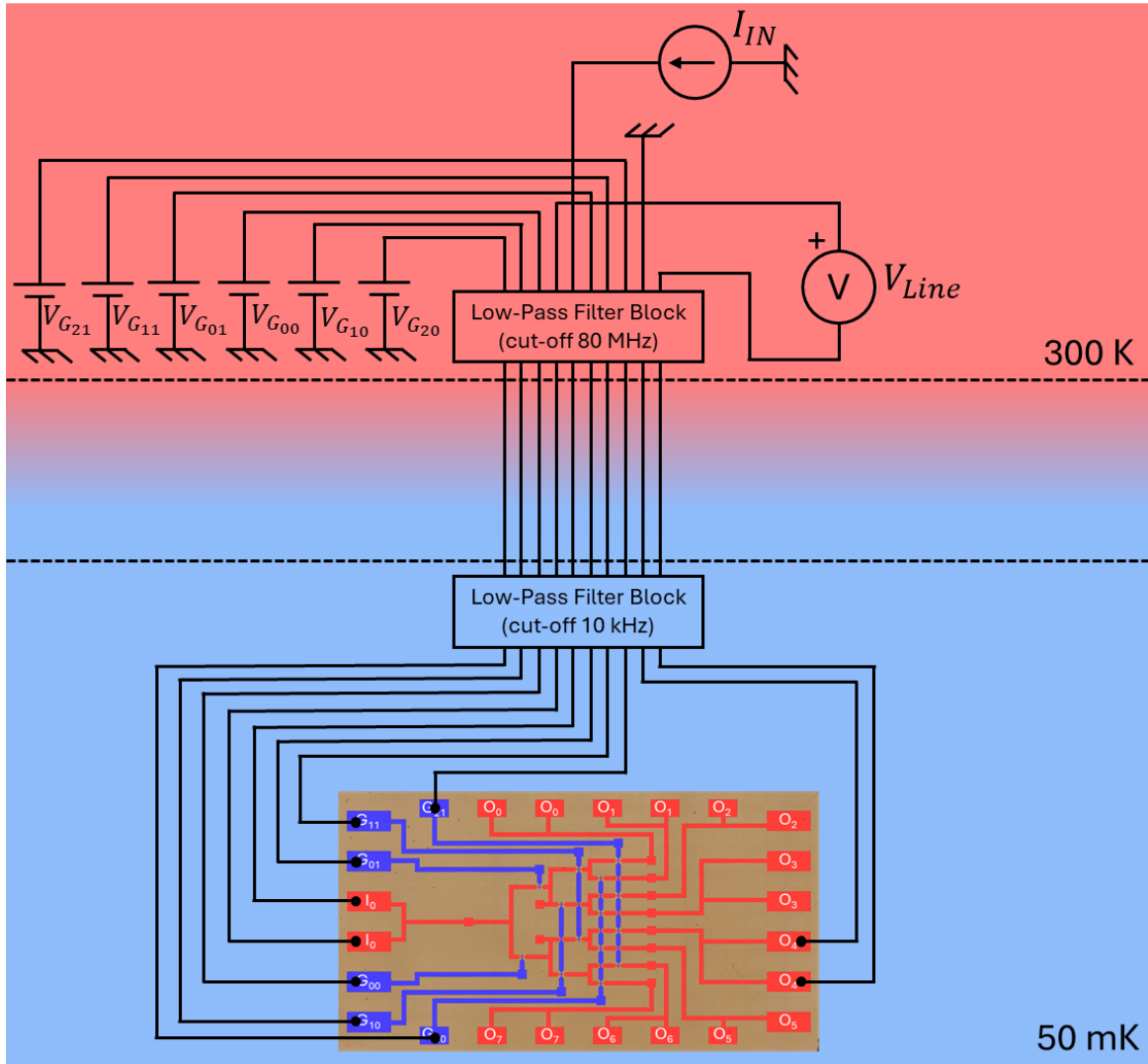
48
49
50
51

Figure S5: Zero-gate-voltage electrical properties of JoFETs. a,b) Switching current (a) and normal state resistance (b) of JoFETs with different gate lengths and interelectrode separations.



52
53
54
55
56
57
58
59
60
61
62
63
64
65
66
67

Figure S6: State of the art of JoFETs. I_S suppression and R_N increase factors achieved for InAsOI-based JoFETs are perfectly in agreement with the top values obtain in the research field.

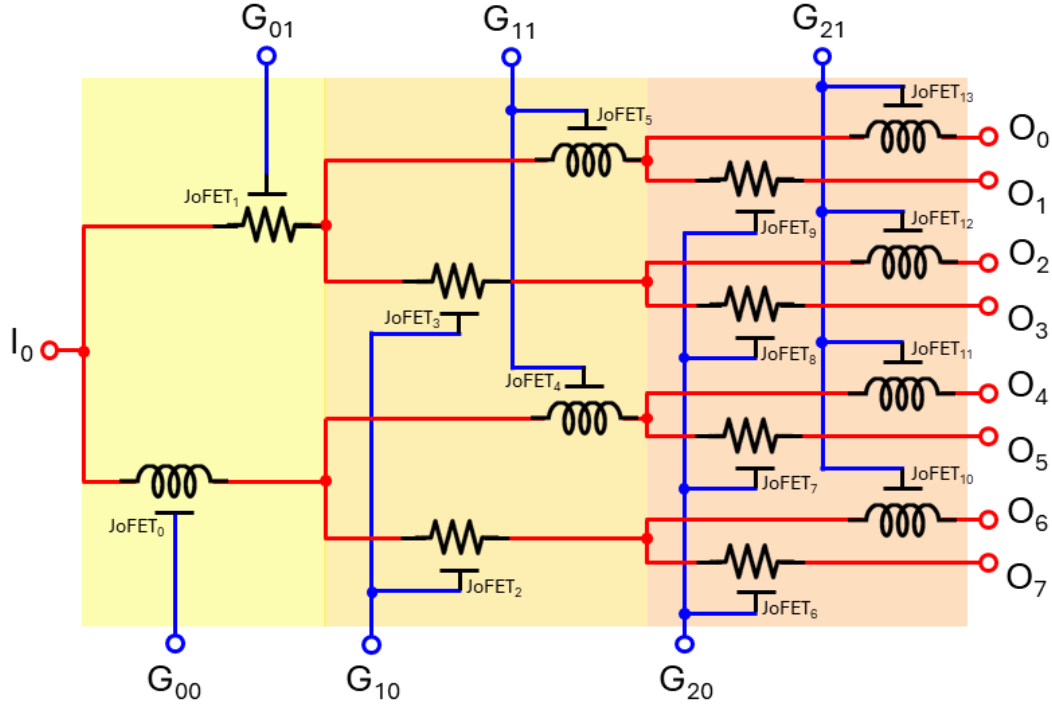


68

69 **Figure S7: DC measurement setup used to characterize the DC electrical behavior of the**
 70 **superconducting 1180 analog demultiplexer.** The input current (I_{IN}) was provided to the
 71 demultiplexer input while the signal line voltage drops (V_{Line}) are measured changing the gate
 72 settings. The figure shows only one line connected.

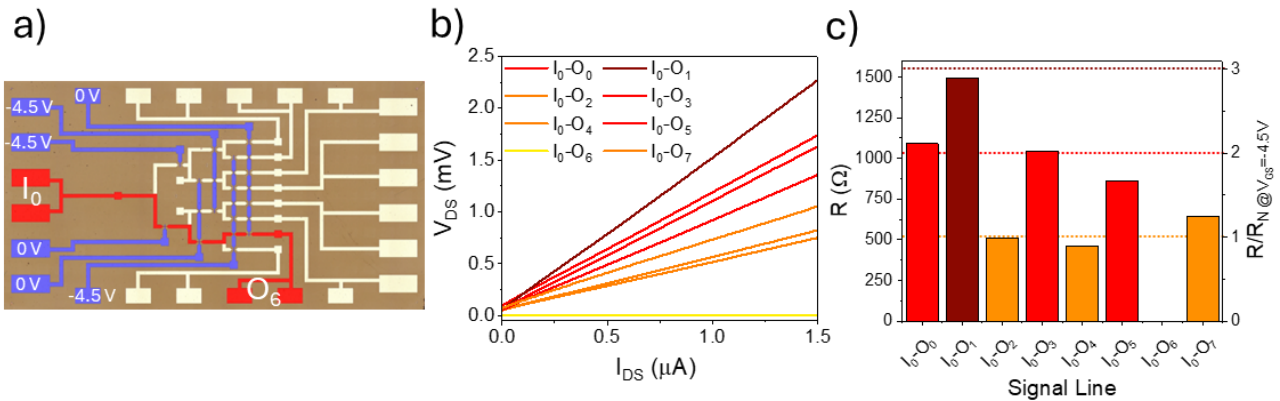
73

74



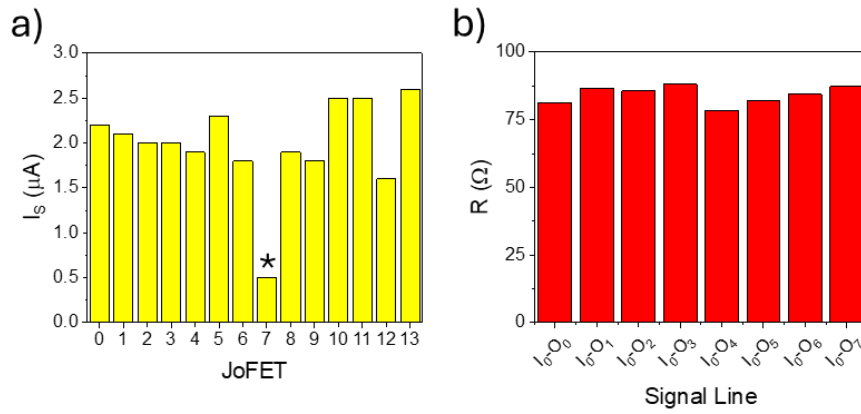
75
76
77
78
79

Figure S8: Schematic lumped elements diagram of the superconducting 1I80 demultiplexer with the signal line I_0 - O_4 in superconducting state. The gate settings are $V_{G00}, V_{G11}, V_{G21} = 0$ V and $V_{G01}, V_{G10}, V_{G20} = -4.5$ V.



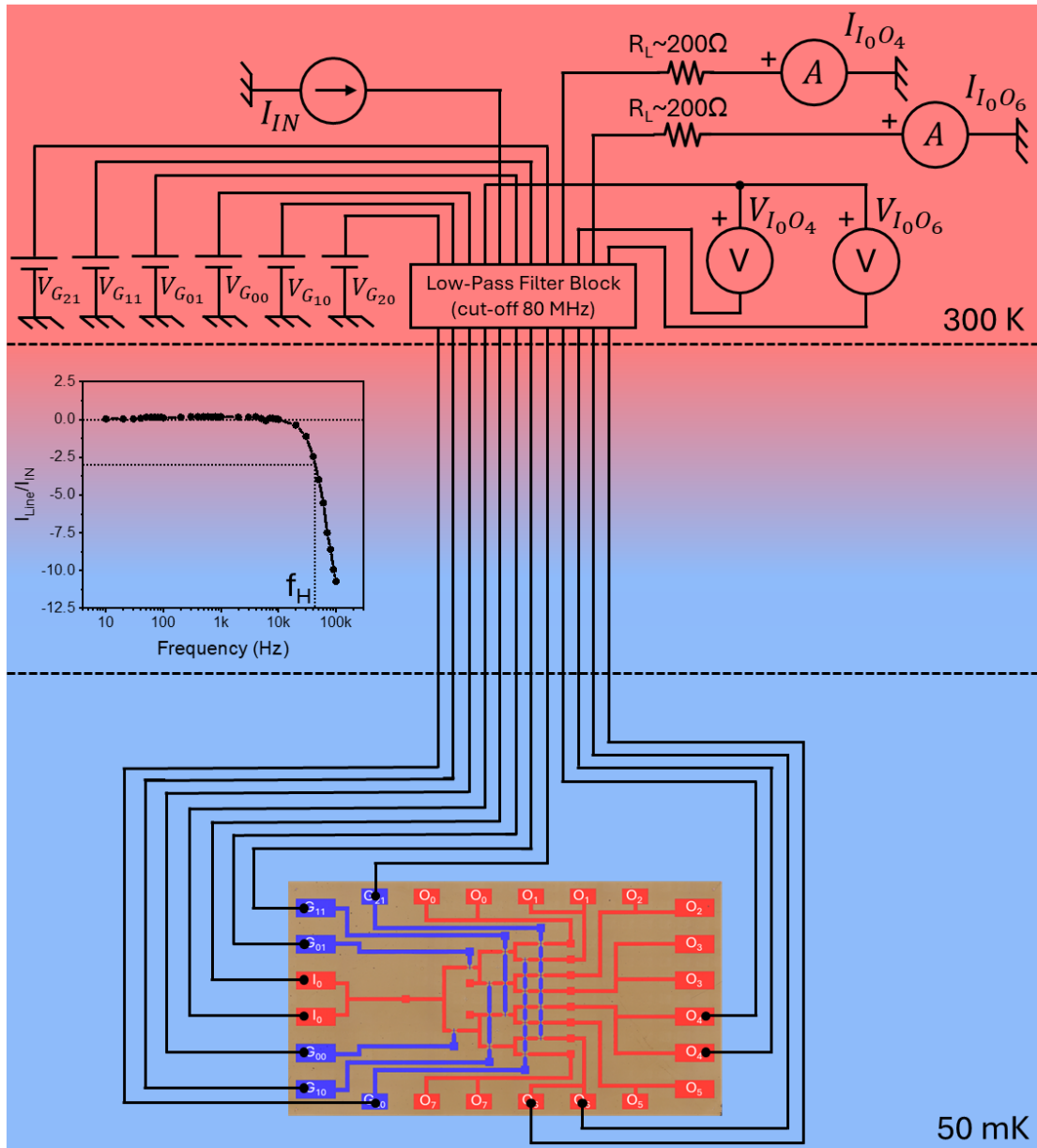
80
81
82
83
84
85
86
87

Figure S9: DC electrical characterization of the superconducting 1I80 demultiplexer with the signal line I_0 - O_6 in superconducting state. a) False-colors optical microscope image of the superconducting 1I80 demultiplexer highlighting the chosen superconductive path and the gate control configuration. b) V-I characteristics of all the 1I80 switch signal lines with the gate configuration shown in (a). Line resistances (left) and normalized line resistances (right) of all the 1I80 demultiplexer signal lines with the gate configuration shown in (a).

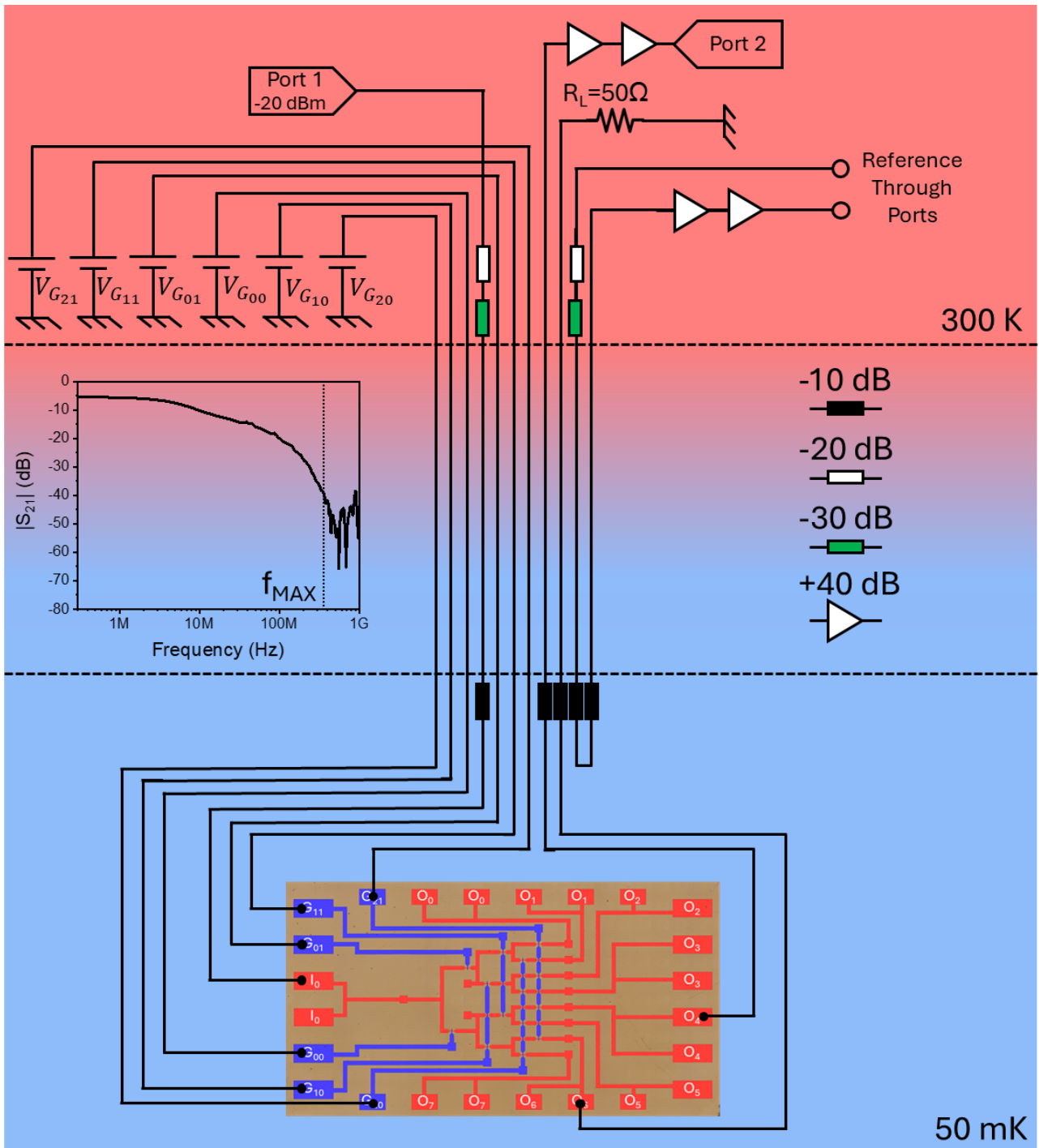


88
 89 **Figure S10: Zero-gate-voltage electrical properties of JoFETs and signal lines of the**
 90 **superconducting 1180 analog demultiplexer.** a) Zero-gate-voltage switching currents of the
 91 JoFETs; only the JoFET₇ exhibits a switching current far from the average. b) Zero-gate-voltage
 92 signal line resistances of the JoFETs.

93
 94
 95
 96
 97

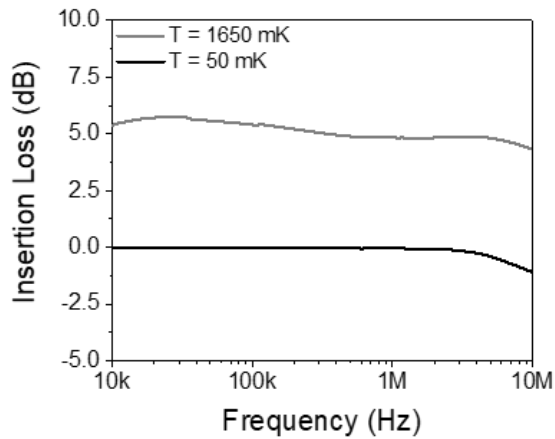


98
 99 **Figure S11: DC-VLF measurement setup used to characterize the real-time electrical**
 100 **behavior of the superconducting 1180 analog demultiplexer.** The input current (I_{IN}) was
 101 provided to the demultiplexer input while the signal line output currents ($I_{I_0 O_4}$ and $I_{I_0 O_6}$) and the
 102 signal line voltage drops ($V_{I_0 O_4}$ and $V_{I_0 O_6}$) are measured changing the gate settings. Cryostat's wires
 103 account as a load resistance of 200 Ω . The system exhibits a cut-off frequency of ~ 45 kHz at 300 K.
 104



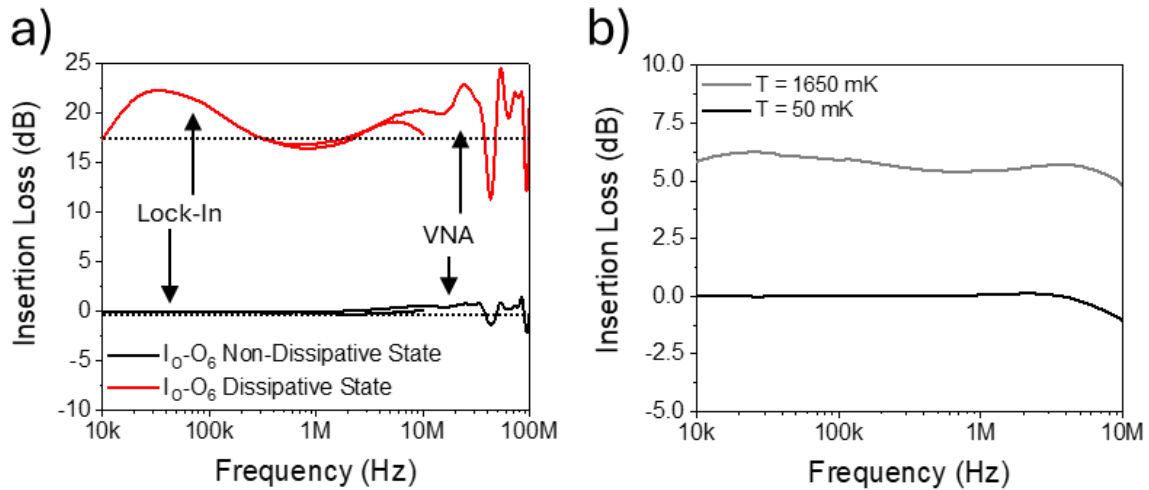
105
106
107
108
109
110
111
112
113
114

Figure S12: LF-VHF measurement setup used to characterize the real-time electrical behavior of the superconducting 1180 analog demultiplexer. The input power ($P_{IN} = -20 \text{ dBm}$) supplied by the Port₁ was attenuated both at 300 K (-50 dB) and 50 mK (-10 dB) then provided to the demultiplexer input. The line O₄ output power was attenuated at 50 mK (-10 dB) and amplified at 300 K (+80 dB) then provided to the Port₂, while line O₆ was terminated with 50 Ω. The output power was measured changing the gate settings. The same was performed to check the line O₆ output power. Reference through ports were used to collect the trough calibration data. The system exhibits a maximum operation frequency of ~300 MHz at 300 K.



115
116
117
118
119

Figure S13: Frequency-resolved insertion loss of signal line I_0-O_4 gated in the non-dissipative state measured at 50 mK and 1650 mK. At 1650 mK, the 1I8O demultiplexer is in the normal state which increases the insertion loss of the signal line.



120
121
122
123
124
125
126
127

Figure S14: Frequency-resolved insertion loss of signal line I_0-O_4 . a) Frequency-resolved insertion loss of signal line I_0-O_6 in the non-dissipative and dissipative states at 50 mK. b) Frequency-resolved insertion loss of signal line I_0-O_6 gated in the non-dissipative state measured at 50 mK and 1650 mK. At 1650 mK, the 1I8O demultiplexer is in the normal state which increases the insertion loss of the signal line.

128
129
130
131
132
133
134

135 **3. Materials and Manufacturing Methods**

136 **3.1 Materials and Chemicals**

137 GaAs wafers (2'' diameter, (100) orientation, $\rho=5.9\times 10^7 \Omega\times\text{cm}$) were purchased from Wafer
138 Technology LTD. Materials used for the Molecular Beam Epitaxy growth (Gallium 7N5,
139 Aluminum 6N5, Indium 7N5, and Arsenic 7N5) were purchased from Azelis S.A.. Acetone (ACE,
140 ULSI electric grade, MicroChemicals), 2-propanol (IPA, ULSI electric grade, MicroChemicals),
141 S1805 G2 Positive Photoresist (S1805, Microposit, positive photoresist), AR-P 679.04 (AllResist,
142 positive e-beam resist), MF319 Developer (MF319, Microposit), AR 600-56 Developer (AR 600-
143 56, AllResist), AR600-71 (AllResist, remover for photo- and e-beam resist), Aluminum Etchant
144 Type D (Transene), Phosphoric acid (H_3PO_4 , Sigma Aldrich, semiconductor grade $\geq 85\%$ in water),
145 Hydrogen peroxide (H_2O_2 , Carlo Erba Reagents, RSE-For electronic use-Stabilized, 30% in water),
146 Nitrogen (N_2 , 5.0, Nippon Gases) was provided by the Clean Room Facility of the National
147 Enterprise for nanoScience and nanotechnology (NEST, Pisa, Italy). Diammonium sulfide
148 $(\text{NH}_4)_2\text{S}$, Carlo Erba Reagents, 20% in water) was provided by the Chemical Lab Facility of the
149 NEST. Sulfur pieces (S, Alfa Aesar, 99.999% pure) was purchased from Carlo Erba Reagents S.r.l.
150 Aluminum pellets (99.999% pure) were purchased from Kurt J. Lesker Company. Aqueous
151 solutions were prepared using deionized water (DIW, $15.0 \text{ M}\Omega\times\text{cm}$) filtered by Elix® (Merck
152 Millipore) provided by the Clean Room Facility of the NEST.

153

154 **3.2 InAsOI Heterostructure Growth via Molecular Beam Epitaxy**

155 InAsOI was grown on semi-insulating GaAs (100) substrates using solid-source Molecular Beam
156 Epitaxy (MBE, Compact 21 DZ, Riber). Starting from the GaAs substrate, the sequence of the layer
157 structure includes a 200 nm-thick GaAs layer, a 200 nm-thick GaAs/ $\text{Al}_{0.16}\text{Ga}_{0.84}\text{As}$ superlattice, a
158 200 nm-thick GaAs layer, a 1.250 μm -thick step-graded $\text{In}_x\text{Al}_{1-x}\text{As}$ metamorphic buffer (with X
159 increasing from 0.15 to 0.81), a 400 nm-thick $\text{In}_{0.84}\text{Al}_{0.16}\text{As}$ overshoot layer, and a 100 nm-thick
160 InAs layer. The GaAs layer and the GaAs/ $\text{Al}_{0.16}\text{Ga}_{0.84}\text{As}$ superlattice below the $\text{In}_x\text{Al}_{1-x}\text{As}$ buffer
161 layer are grown to planarize the starting GaAs surface and to reduce surface roughness caused by
162 the oxide desorption process. Both are grown with a group V/III beam flux ratio of 6.

163 The metamorphic buffer consists of two regions with different misfit gradients. The first $\text{In}_x\text{Al}_{1-x}$ -
164 As region is composed of twelve 50 nm-thick layers with X ramping from 0.15 to 0.58. The
165 second $\text{In}_x\text{Al}_{1-x}\text{As}$ region is composed of twelve 50 nm-thick layers with X ramping from 0.58 to
166 0.81. The Al flux was kept constant during the buffer layer growth, while the In flux was increased
167 at each step without growth interruptions. At the end of the buffer, the overshoot layer was grown to
168 increase the strain relaxation of the $\text{In}_x\text{Al}_{1-x}\text{As}$ metamorphic layer [37]. The As flux was adjusted

169 during the growth of the metamorphic buffer and the overshoot layer to keep a constant group V/III
170 beam flux ratio of 8. The InAs layer was growth with a group V/III beam flux ratio of 8 and a
171 growth rate of 0.96 $\mu\text{m}/\text{h}$. The GaAs layer and GaAs/AlGaAs superlattice are grown at $600\text{ }^\circ\text{C} \pm 5$
172 $^\circ\text{C}$. The metamorphic buffer and the overshoot layers were grown at optimized substrate
173 temperatures of $320\text{ }^\circ\text{C} \pm 5\text{ }^\circ\text{C}$. The InAs epilayer was grown at $480 \pm 5\text{ }^\circ\text{C}$.

174

175 In the following, all wetting steps were performed in cleaned glass Beckers using stainless steel
176 tweezers provided with carbon tips. Teflon-coated tweezers were used for all the steps requiring
177 acid or base solutions. The Julabo TW2 was used to heat the solution to a specific temperature.

178

179 **3.3 InAsOI Josephson Field Effect Transistor Fabrication**

180 Superconductor Deposition on InAsOI

181 InAsOI substrates were cut into square samples ($7 \times 7\text{ mm} \times \text{mm}$) and sonicated in ACE and IPA for 5
182 min to remove GaAs dusts. The air-exposed InAs surface was etched from native InAs oxide
183 (InAsO_x) and passivated with S-termination by dipping the InAsOI samples in a $(\text{NH}_4)_2\text{S}_x$ solution
184 ($290\text{ mM } (\text{NH}_4)_2\text{S}$ and 300 mM S in DIW) at 45°C for 90 s. The S-terminated InAsOI samples were
185 then rinsed twice in DIW for 30 s and immediately loaded ($\sim 90\text{ s}$ exposure time in the air) into the
186 load-lock vacuum chamber of an e-beam evaporator (acceleration voltage 7 kV). Samples were
187 transferred into the deposition chamber, where a 100-nm-thick Al layer was deposited at a rate of 2
188 A/s at a residual chamber pressure of $1\text{E}-8 \div 5\text{E}-9\text{ Torr}$.

189 InAsOI MESA Fabrication

190 After Al deposition, a layer of S1805 positive photoresist was spin-coated at 5000 RPM for 60 s
191 (spin coating acceleration of 5000 RPM/s) and soft-baked at $115\text{ }^\circ\text{C}$ for 60 s. The resist was then
192 exposed via direct writing UV lithography (UVL, DMO, ML3 laser writer, $\lambda=385\text{ nm}$) with a dose
193 of 60 mJcm^{-2} , resolution of $0.6\text{ }\mu\text{m}$, high exposure quality, and laser-assisted real-time focus
194 correction to define the MESA geometry. Unless otherwise stated, all the rinsing steps were
195 performed at room temperature (RT, $21\text{ }^\circ\text{C}$). The UV-exposed samples were developed in MF319
196 for 45 s with soft agitation to remove exposed photoresist, then rinsed in DIW for 30 s to stop the
197 development and dried with N_2 . The exposed Al layer was removed by dipping the sample in Al
198 Etchant Type D at $40\text{ }^\circ\text{C}$ for 65 seconds with soft agitation, then rinsed in DIW for 30 seconds to
199 stop the etching and dried with N_2 . The exposed InAs epilayer was etched by dipping the samples in
200 a $\text{H}_3\text{PO}_4:\text{H}_2\text{O}_2$ solution ($348\text{ mM H}_3\text{PO}_4$, $305\text{ mM H}_2\text{O}_2$ in DIW) for 60 s with soft agitation, then
201 rinsed in DIW for 30 s to stop the etching and dried with N_2 . Eventually, the photoresist was

202 removed by rinsing the InAsOI samples in ACE at 60 °C for 5 minutes and IPA for 60 s, then dried
203 with N₂. At the end of this step, the width (W) of the JoFET was set to 5 μm.

204 Markers Deposition for Aligned Steps

205 After MESA fabrication, a layer of AR-P 679.04 positive e-beam resist was spin-coated at 4000
206 RPM for 60 s (spin coating acceleration of 10000 RPM/s) and soft-baked at 160 °C for 60 s. The
207 resist was then exposed via UVL-marker-aligned e-beam lithography (EBL, ZEISS, Ultra Plus)
208 with a dose of 350 μCcm⁻², voltage acceleration of 30 kV, aperture of 7.5 or 120 μm, line step size
209 of 1 nm or 200 nm, to define EBL-markers for the next alignment steps. The electron-exposed
210 samples were developed in AR 600-56 for 90 s with soft agitation to remove the exposed e-beam
211 resist, then rinsed in IPA for 30 s to stop the development and dried with N₂. The samples were
212 loaded into a thermal evaporator (Sistec prototype) where a 10/50-nm-thick Ti/Au bilayer was
213 deposited at a rate of 1 Å/s at a residual chamber pressure of 2E-6 mbar. The deposited film was
214 lifted-off in ACE at 70 °C for 5 min with strong agitation, then rinsed in IPA for 60 s, and dried
215 with N₂.

216 Aligned Josephson Junction Fabrication

217 After EBL marker definition, a layer of AR-P 679.04 positive e-beam resist was spin-coated at 4000
218 RPM for 60 s (spin coating acceleration of 10000 RPM/s) and soft-baked at 160 °C for 60 s. The
219 resist was then exposed via marker-aligned EBL (ZEISS, Ultra Plus) with a dose of 350 μCcm⁻²,
220 voltage acceleration of 30 kV, aperture of 7.5 μm, and line step size of 1 nm to define the Josephson
221 junction length (L_{JJ}). The electron-exposed samples were developed in AR 600-56 for 90 s with soft
222 agitation to remove the exposed e-beam resist, then rinsed in IPA for 30 s to stop the development
223 and dried with N₂. Subsequently, the exposed Al layer was removed by dipping the sample in Al
224 Etchant Type D at 40 °C for 65 seconds with soft agitation, then rinsed in DIW for 30 seconds to
225 stop the etching and dried with N₂. Eventually, the e-beam resist was removed by rinsing the
226 InAsOI samples in ACE at 70 °C for 5 min, IPA for 60 s, and dried with N₂. At the end of this step,
227 we achieved L_{JJ} ranging from 500 to 1250 nm.

228 Gate Insulator Deposition

229 Samples were loaded into the vacuum chamber of an Atomic Layer Deposition system (ALD,
230 Oxford Instruments, OpAL) where the gate insulator was uniformly deposited at a temperature of
231 130 °C. Tetrakis(ethylmethylamino)hafnium (TEMAH) and H₂O were used as HfO₂ precursors,
232 while Ar was used as carrier gas. Ar bubbling was also involved to increase the volatility of
233 TEMAH. After reaching a base pressure of ~3-4 mTorr, the chamber pressure was increased to
234 ~350 mTorr injecting Ar. The deposition process follows 4 steps: (i) TEMAH dose, (ii) TEMAH
235 purge, (iii) H₂O dose, and (iv) H₂O purge:

- 236 (i) TEMAH dose: TEMAH valve on; Ar bubbler: 250 sccm; Ar purge: 10 sccm; step
237 duration: 0.9 s.
- 238 (ii) TEMAH: purge: TEMAH valve off; Ar purge: 250 sccm; step duration: 110 s.
- 239 (iii) H₂O dose: H₂O valve on; Ar purge: 10 sccm; step duration: 0.03 s.
- 240 (iv) H₂O purge: H₂O valve off; Ar purge: 250 sccm; step duration: 90 s.

241 We performed 250 ALD cycles to achieve a total insulator thickness of ~31 nm [39]. Eventually,
242 the chamber was pumped to reach a base pressure of ~3-4 mTorr and then vented using N₂. The
243 entire process takes ~16 h.

244 Aligned Metal Gate Deposition

245 After gate insulator deposition, a layer of AR-P 679.04 positive e-beam resist was spin-coated at
246 4000 RPM for 60 s (spin coating acceleration of 10000 RPM/s) and soft-baked at 160 °C for 60 s.
247 The resist was then exposed via marker-aligned EBL (ZEISS, Ultra Plus) with a dose of 350 μCcm^{-2} ,
248 voltage acceleration of 30 kV, aperture of 7.5 or 120 μm , line step size of 1 or 200 nm, to define
249 the JoFET gate length (L_G). The electron-exposed samples were developed in AR 600-56 for 90 s
250 with soft agitation to remove the exposed e-beam resist, then rinsed in IPA for 30 s to stop the
251 development and dried with N₂. Samples were mounted into an e-beam evaporator (acceleration
252 voltage 7 kV), where a 10/100-nm-thick Ti/Al bilayer was deposited at a rate of 0.5/2 A/s with a tilt
253 angle of 53° at a residual chamber pressure of 1E-8 ÷ 1E-9 Torr. The deposited film was lifted-off
254 in AR600-71 at 80 °C for 5 min with strong agitation, then rinsed in IPA for 30 s, and dried with
255 N₂.

256
257
258
259
260
261
262
263
264
265
266
267
268
269

270 **3.4 InAsOI Superconducting 1180 Demultiplexer Fabrication**

271 Superconductor Deposition on InAsOI

272 This step was performed in agreement with what reported in Section 3.3 “InAsOI Josephson Field
273 Effect Transistor Fabrication: Superconductor Deposition on InAsOI”.

274 InAsOI MESA Fabrication

275 This step was performed in agreement with what reported in Section 3.3 “InAsOI Josephson Field
276 Effect Transistor Fabrication: InAsOI MESA Fabrication”.

277 Aligned Josephson Junction Fabrication

278 This step was performed in agreement with what reported in Section 3.3 “InAsOI Josephson Field
279 Effect Transistor Fabrication: Aligned Josephson Junction Fabrication” using UVL markers defined
280 in the previous step instead of EBL markers.

281 Gate Insulator Deposition

282 This step was performed in agreement with what reported in Section 3.3 “InAsOI Josephson Field
283 Effect Transistor Fabrication: Gate Insulator Deposition”.

284 Aligned Metal Gate Deposition

285 After the insulator deposition, samples were removed from the ALD system and heated up to 170
286 °C for 180 s to desorb adsorbed water molecules from air. After that, a LOR3A/S1805 bilayer was
287 deposited. LOR3A was spin-coated at 4000 RPM for 60 s (spin coating acceleration of 4000
288 RPM/s) and soft-baked at 170 °C for 180 s. The LOR3A spin coating and soft bake procedure was
289 performed 2 times to increase the LOR3A thickness. Then, S1805 positive photoresist was spin-
290 coated at 5000 RPM for 60 s (spin coating acceleration of 5000 RPM/s) and soft-baked at 115 °C
291 for 60 s. The resist was exposed via direct writing UV lithography (UVL, DMO, ML3 laser writer,
292 $\lambda=385$ nm) with a dose of 60 mJcm^{-2} , resolution of $0.6 \mu\text{m}$, high exposure quality, and no real-time
293 focus correction to define gate pattern. The UV-exposed samples were developed in MF319 for 120
294 s with soft agitation to remove exposed S1805 and the underlying layer of LOR3A, then rinsed in
295 DIW for 30 s to stop the development and dried with N_2 .

296 Samples were mounted into an e-beam evaporator (acceleration voltage 7 kV), where a 10/250-nm-
297 thick Ti/Al bilayer was deposited at a rate of $0.5/2 \text{ A/s}$ at a residual chamber pressure of $1\text{E}-8 \div 1\text{E}-$
298 9 Torr . The evaporation was performed with the following tilt angles: (i) 0° for 10 nm Ti and 100
299 nm Al; (ii) -45° for 75 nm Al; (iii) 45° for 75 nm Al. The deposited film was lifted-off in AR600-71
300 at $80 \text{ }^\circ\text{C}$ for 5 min with strong agitation, then rinsed in IPA for 30 s, and dried with N_2 .

301

302

303
304
305
306
307
308
309
310
311
312
313
314
315
316
317
318
319
320
321
322
323
324
325
326
327
328
329
330
331
332
333
334
335
336

3.5 InAsOI Hall Bars Fabrication

Metal Deposition on InAsOI

This step was performed in agreement with what reported in Section 3.3 “InAsOI Josephson Field Effect Transistor Fabrication: Superconductor Deposition on InAsOI”.

Metal Pads Fabrication

After Al deposition, a layer of S1805 positive photoresist was spin-coated at 5000 RPM for 60 s (spin coating acceleration of 5000 RPM/s) and soft-baked at 115 °C for 60 s. Then, the photoresist was exposed via direct writing UV lithography (DMO ML3 laser writer, $\lambda=385$ nm) with a dose of 60 mJcm⁻², resolution of 0.6 μ m, high exposure quality, and laser-assisted real-time focus correction to define the Al geometry for fabrication of 6-terminals Hall Bars. Unless stated otherwise, all the rinsing steps were performed at room temperature (RT, 21 °C). The UV-exposed samples were developed in MF319 for 45 s with soft agitation to remove exposed photoresist, then rinsed in DIW for 30 s to stop the development and dried with N₂. The exposed Al layer was removed by dipping the sample in Al Etchant Type D at 40 °C for 65 seconds with soft agitation, then rinsed in DIW for 30 seconds to stop the etching and dried with N₂. Eventually, the photoresist was removed by rinsing the InAsOI samples in ACE at 60 °C for 5 min and IPA for 60 s, which was then dried with N₂.

InAsOI MESA Fabrication

A layer of S1805 positive photoresist was spin-coated at 5000 RPM for 60 s (spin coating acceleration of 5000 RPM/s) and soft-baked at 115 °C for 60 s. Then, the photoresist was exposed via a second marker-aligned direct writing UV lithography (DMO ML3 laser writer, $\lambda=385$ nm) with a dose of 60 mJcm⁻², resolution of 0.6 μ m, high exposure quality, and no real-time focus correction, to define the InAs/InAlAs geometry for fabrication of Hall Bars. The UV-exposed samples were developed in MF319 for 45 s with soft agitation to remove exposed photoresist, then rinsed in DIW for 30 s to stop the development and dried with N₂. Then, the exposed InAs epilayer was etched by dipping the samples in a H₃PO₄:H₂O₂ solution (348 mM H₃PO₄, 305 mM H₂O₂ in DIW) for 60 s with soft agitation, then rinsed in DIW for 30 s to stop the etching and dried with N₂. Eventually, the photoresist was removed by rinsing the InAsOI samples in ACE at 60 °C for 5 min, IPA for 60 s, and drying with N₂. We fabricated 6-contact Hall bars with a width of 100 μ m, source-to-drain length of 500 μ m, and probe-to-probe length of 250 μ m.

337
338
339
340
341
342
343
344
345
346
347
348
349
350
351
352
353
354
355
356
357
358
359
360
361
362
363
364
365
366
367
368
369
370

3.6 Sample Bonding via Wire Wedge Bonding

All the fabricated samples were provided with bonding pads ranging from 150×150 to 200×200 $\mu\text{m} \times \mu\text{m}$ and then used to connect the device with the chip carrier. Samples were glued using a small drop of AR-P 679.04, then left dry at RT for 1 hour on a 24-pin dual-in-line (DIL) chip carrier. Samples were bonded via wire wedge bonding (MP iBond5000 Wedge) using an Al/Si wire (1%, 25 μm wire diameter), leaving the user-bonder and the DIL chip carrier electrically connected to the ground.

4. Characterization Methods

4.1 Morphological Characterization

via Scanning Electron Microscopy

Top view morphological characterization of JJs was carried out via scanning electron microscopy (SEM, ZEISS Merlin) with 5 kV acceleration voltage, 178 pA filament current, back scattered electron relevator, at different magnifications (2.5k and 50k).

via Optical Microscopy

Optical microscopy (Leica, DM8000 M, provided with LEICA MC190 HD camera) was used to verify all the steps without photoresist. An optical microscope (Nikon, Eclipse ME600, provided with Nikon TV Lens C-0.6 \times and a UV filter) was used to evaluate all the steps involving the photoresist.

via Atomic Force Microscopy

Atomic force microscopy (AFM, Bruker, DIMENSION edge with ScanAsyst provided with an ASYLEC-01-R2 tip - silicon tip Ti/Ir coated, $f_0=75$ kHz, $k=2.8$ N/m - in tapping mode) was used to evaluate the profile of the fabricated JoFETs. All the AFM photos were processed using Gwyddion.

371

372 **4.2 Electrical Characterization**

373 *4.2.1 Cryogenic DC Electrical Characterization of InAsOI Josephson Field Effect Transistors*

374 Electrical characterization of JoFETs was carried out by measuring 4-wires V-I curves at 50 mK.
375 Out-of-plane magnetic field (B_{\perp}) was used to maximize the switching current at 0 gate voltage, then
376 maintained for all the characterization. The sample was mounted in contact with the mixing
377 chamber (MC) plate of the Leiden CF-CS81-1400 cryostat. Electrical configuration of the
378 measurement setup is shown in **Figure S3**. Source-drain current (I_{DS}) was injected applying an
379 increasing DC voltage (Voltage Source, YOKOGAWA GS200) over an input series resistor ($R= 1$
380 $M\Omega$) at least 100 times larger than the total resistance of the remaining measurement setup. The
381 voltage drop across the probe contacts (V_{DS}) was amplified (Voltage Amplifier, DL Instruments
382 1201, Gain = 10k, High pass filter = DC, Low pass filter = 100 Hz) and read (Multimeter, Agilent,
383 34410A, NPLC = 2). The gate-source voltage (V_{GS}) was changed between 0 and -4.5 V (SMU,
384 Keithley, 2400).

385 The switching current (I_S) was estimated as the last applied current in the V-I curve before reading a
386 voltage drop different from the noise floor, while the normal state resistance (R_N) was evaluated as
387 the angular coefficient of the V-I linear best fitting curve for $I > I_S$.

388 Gate current leakage was evaluated measuring the gate I-V curve (with source terminal grounded
389 and the other terminals left open) upon application of an increasing voltage (SMU, Keithley, 2400,
390 absolute voltage step = 100 mV, step delay = 1 s) and collecting the flowing current (TIA, FEMTO,
391 DDPCA-300, gain = 10^{10} V/A, rise time = fast; Multimeter, Agilent, 34410A, NPLC = 2).

392

393 *4.2.2 Cryogenic Electrical Characterization of the Superconducting I180 Analog Demultiplexer*

394 DC Electrical Characterization

395 DC electrical characterization of the signal lines was carried out by measuring 4-wires V-I curves at
396 50 mK. The sample was mounted in contact with the mixing chamber (MC) plate of the Oxford
397 Triton 200. Electrical configuration of the measurement setup is shown in **Figure S7**. Signal line
398 input current (I_{IN}) was injected into the I_0 terminal applying an increasing DC voltage (Voltage
399 Source, YOKOGAWA GS200) over an input series resistor ($R= 1 M\Omega$) at least 100 times larger
400 than the total resistance of the remaining measurement setup. The voltage drop across the probe
401 contacts of the signal line (V_{Line}) was amplified (Voltage Amplifier, DL Instruments 1201, Gain =
402 10k, High pass filter = DC, Low pass filter = 100 Hz) and read (Multimeter, Agilent, 34410A,

403 NPLC = 1). Gate control voltages (V_{Gij}) were changed between 0 and -4.5 V (SMU, Keithley,
404 2400). Terminals of other lines were left open during the measurement.

405 Each signal line features 3 different I_S of the 3 JoFETs along the path. I_S were estimated as the last
406 applied current in the V-I curve before reading a step in the voltage drop, while the signal line
407 resistance (R) was evaluated as the angular coefficient of the V-I linear best fitting curve for input
408 currents larger than the third switching current detected.

409 Gate current leakage was evaluated measuring the gate I-V curve (with I_0 terminal grounded and the
410 other terminals left open) upon application of an increasing voltage (SMU, Keithley, 2400, absolute
411 voltage step = 100 mV, step delay = 1 s) and collecting the flowing current (TIA, DL, 1211,
412 gain= 10^{10} V/A, rise time = 0.3 s; Multimeter, Agilent, 34410A, NPLC = 2).

413 Real-Time Electrical Characterization

414 Real-time electrical characterization of the signal lines I_0O_4 and I_0O_6 was carried out by measuring
415 4-wires V-I curves at 50 mK. Electrical configuration of the measurement setup is shown in **Figure**
416 **S10**. Signal line input current (I_{IN}) of $\sim 1.3 \mu\text{A}$ was injected into the I_0 terminal applying an DC
417 voltage of 1.3 V (Voltage Source, YOKOGAWA GS200) over an input series resistor ($R = 1 \text{ M}\Omega$) at
418 least 100 times larger than the total resistance of the remaining measurement setup. Voltage drops
419 across the probe contacts of each signal line (V_{Line}) was amplified (Voltage Amplifier, DL
420 Instruments 1201, Gain = 500, High pass filter = DC, Low pass filter = MAX) and real-time
421 collected (Oscilloscope, Tektronix, TDS2024B, averages = 128). The current flowing in each signal
422 line (I_{Line}) was also measured (TIA, DL, 1211, gain= 10^5 V/A, rise time = min; Oscilloscope,
423 Tektronix, TDS2024B, averages = 128). Gate control voltages (V_{Gij}) were changed between 0 and -
424 4.5 V (SMU, Keithley, 2400). Terminals of other lines were left open during the measurement. The
425 cryostat's wires account as a load resistance of $\sim 200 \Omega$.

426 VLF AC Electrical Characterization

427 VLF AC electrical characterization of the signal line I_0O_4 was carried out by measuring 4-wires V-I
428 curves at 50 mK. A signal line input current (I_{IN}) with 1 kHz frequency and peak-to-peak values
429 from 2 to 16 μA was injected into the I_0 terminal applying an AC voltage (Wavefunction Generator,
430 Agilent, 33220A) over an input series resistor ($R = 1 \text{ M}\Omega$) at least 100 times larger than the total
431 resistance of the remaining measurement setup. Voltage drops across the probe contacts of the
432 signal line I_0O_4 was amplified (Voltage Amplifier, DL Instruments 1201, Gain = 500, High pass
433 filter = DC, Low pass filter = MAX) and real-time collected (Oscilloscope, Tektronix, TDS2024B,

434 averages = 128). Gate control terminals and other signal line terminals were left open during the
435 measurement.

436

437

438 LF-UHF AC Electrical Characterization

439 VLF-HF AC electrical characterization of signal lines I_0O_4 and I_0O_6 was carried using a lock-in
440 amplifier (Lock-in, Zurich Instruments, UHF Lock-in Amplifier 600 MHz, 1.8 GSa/s) at 50 and
441 1650 mK. Electrical configuration of the measurement setup is shown in **Figure S11**. The output
442 port of the lock-in (Port1, power -20 dBm, frequency 10 kHz - 10 MHz) was attenuated by -50 dB
443 at 300 K and -10 dB on the mixing chamber (MC), then provided as input power of the
444 demultiplexer to the I_0 terminal. Then, the signal line output power was attenuated by -10 dB on the
445 MC, amplified by +80 dB at 300 K (FEMTO, HSA-X-I-2-40), and provided to input port (Port2,
446 averages = 25) of the lock-in. When measuring the signal line I_0O_4 , the I_0O_6 was terminated to 50
447 Ω , and vice versa. To retrieve the “through” calibration file of the measurement system, two
448 cryostat ports were connected with a feed-through connector on the MC and provided with the same
449 attenuation and amplification of the measurement lines. For both the signal line ($r_{\text{line+sys}}$) and
450 calibration (r_{sys}) measurements, we collected the magnitude of the voltage measured by the lock-in
451 (r). The forward power gain scattering parameter, i.e., the $|S_{21}|$ (dB), of the signal line was obtained
452 as $|S_{21}| = 20\log(r_{\text{line+sys}}/r_{\text{sys}})$. Gate control voltages (V_{Gij}) were changed between 0 and -4.5 V (SMU,
453 Keithley, 2400).

454 MF-VHF AC electrical characterization of signal lines I_0O_4 and I_0O_6 was carried using a vector
455 network analyzer (VNA, PicoTech, PicoVNA 108) at 50 mK. Electrical configuration of the
456 measurement setup is shown in **Figure S11**. The Port1 of the VNA (power -20 dBm, frequency 300
457 kHz - 100 MHz) was attenuated by -50 dB at 300 K and -10 dB on the mixing chamber (MC), then
458 provided as input power of the demultiplexer to the I_0 terminal. Then, the signal line output power
459 was attenuated by -10 dB on the MC, amplified by +80 dB at 300 K (FEMTO, HSA-X-I-2-40), and
460 provided to the Port2 (bandwidth = 1 kHz) of the VNA. When measuring the signal line I_0O_4 , the
461 I_0O_6 was terminated to 50 Ω , and vice versa. To retrieve the “through” calibration file of the
462 measurement system, two cryostat ports were connected with a feed-through connector on the MC
463 and provided with the same attenuation and amplification of the measurement lines. For both the
464 signal line ($|S_{21}|_{\text{line+sys}}$) and calibration ($|S_{21}|_{\text{sys}}$) measurements, we collected the $|S_{21}|$ parameter. The
465 $|S_{21}|$ (dB) of the signal line was obtained as $|S_{21}|_{\text{line}} = |S_{21}|_{\text{line+sys}} - |S_{21}|_{\text{sys}}$. Gate control voltages (V_{Gij})
466 were changed between 0 and -4.5 V (SMU, Keithley, 2400).

467
468
469
470
471
472
473
474
475
476
477
478
479
480
481
482
483
484
485
486
487
488
489
490
491
492
493
494
495
496
497
498
499

4.2.3 Cryogenic and Room Temperature Electrical Characterization of InAsOI

Hall measurements were performed on Hall Bars (HBs) with a standard lock-in-amplifier-based technique. The first lock-in amplifier oscillator voltage ($V_{OSC,RMS} = 1 \text{ V}$, $f = 13.321 \text{ Hz}$) was applied across a series resistor ($R=10 \text{ M}\Omega$) at least 100 times larger than the total resistance of the remaining measurement setup to use the AC current ($I_{OSC,RMS}$). The AC current is injected into the sample's source contact. In contrast, the flowing current is measured with the drain contact, and the second lock-in amplifier measures the voltage drop's magnitude and phase across two other contacts. The contacts are manually switched to inject the current and measure the voltage. The Hall measurements were performed in three steps. In the first step, the resistivity (ρ) is calculated at zero magnetic fields using the formula $\rho = R_{xx} \times \frac{W \times t}{l}$, where R_{xx} is the resistance measured between longitudinal (same-side) contacts of the HB for a current passing between source and drain, W is the HB width, t is the InAs thickness, and l is the distance between probe contacts. In the second and third steps, the Hall voltage (V_H) is measured by applying positive and negative out-of-plane magnetic fields ($|B| = 250 \text{ mT}$), respectively. V_H is measured between opposite probe contacts of the HB for a current passing through the source and drain. The sheet electron density (n_{2D}) is calculated using the formula $n_{2D} = \frac{n_{2D}^1 + n_{2D}^2}{2}$, with $n_{2D}^i = \frac{I_{OSC,RMS} \times B_i}{q \times V_H}$, where q is the fundamental charge, and B_i is the magnitude of the applied out-of-plane magnetic field. The electron mobility (μ_n) is calculated using the formula $\mu_n = \frac{\mu_n^1 + \mu_n^2}{2}$, with $\mu_n^i = \frac{1}{n_{2D}^i \times q \times R_{xx}}$.

500
501
502
503
504
505
506
507
508
509
510
511
512
513
514
515
516
517
518
519
520
521
522
523
524
525
526
527
528
529
530
531
532
533
534
535
536
537
538
539
540
541

References

- [1] H. Takayanagi, J.B. Hansen, J. Nitta, Localization Effects on the Critical Current of a Superconductor—Normal-Metal—Superconductor Junction, *Phys. Rev. Lett.* 74 (1995) 162–165. <https://doi.org/10.1103/PhysRevLett.74.162>.
- [2] A. Chrestin, R. Kürsten, K. Biedermann, T. Matsuyama, U. Merkt, Superconductor/semiconductor nanostructures on p-type InAs, *Superlattices Microstruct.* 25 (1999) 711–720. <https://doi.org/10.1006/spmi.1999.0719>.
- [3] T. Akazaki, J. Nitta, H. Takayanagi, K. Arai, Superconducting junctions using a 2DEG in a strained InAs quantum well inserted into an InAlAs/InGaAs MD structure, *IEEE Trans. Applied Supercond.* 5 (1995) 2887–2891. <https://doi.org/10.1109/77.403195>.
- [4] H. Takayanagi, T. Akazaki, J. Nitta, T. Enoki, Superconducting Three-Terminal Devices Using an InAs-Based Two-Dimensional Electron Gas, *Jpn. J. Appl. Phys.* 34 (1995) 1391. <https://doi.org/10.1143/JJAP.34.1391>.
- [5] H. Takayanagi, T.A. Tatsushi Akazaki, Submicron Gate-Fitted Superconducting Junction Using a Two-Dimensional Electron Gas, *Jpn. J. Appl. Phys.* 34 (1995) 6977. <https://doi.org/10.1143/JJAP.34.6977>.
- [6] T. Akazaki, H. Takayanagi, J. Nitta, T. Enoki, A Josephson field effect transistor using an InAs-inserted-channel In_{0.52}Al_{0.48}As/In_{0.53}Ga_{0.47}As inverted modulation-doped structure, *Appl. Phys. Lett.* 68 (1996) 418–420. <https://doi.org/10.1063/1.116704>.
- [7] T. Akazaki, J. Nitta, H. Takayanagi, T. Enoki, Superconducting transistors using InAs-inserted-channel InAlAs/InGaAs inverted HEMTs, *Supercond. Sci. Technol.* 9 (1996) A83–A86. <https://doi.org/10.1088/0953-2048/9/4A/022>.
- [8] A. Richter, M. Koch, T. Matsuyama, U. Merkt, Transport properties of Nb/InAs(2DEG)/Nb Josephson field-effect transistors, *Supercond. Sci. Technol.* 12 (1999) 874–876. <https://doi.org/10.1088/0953-2048/12/11/354>.
- [9] A. Richter, P. Baars, U. Merkt, Supercurrents in two-dimensional electron systems, *Phys. E Low-Dimensional Syst. Nanostructures.* 12 (2002) 911–917. [https://doi.org/10.1016/S1386-9477\(01\)00408-8](https://doi.org/10.1016/S1386-9477(01)00408-8).
- [10] J. Shabani, M. Kjaergaard, H.J. Suominen, Y. Kim, F. Nichele, K. Pakrouski, T. Stankevic, R.M. Lutchyn, P. Krogstrup, R. Feidenhans'l, S. Kraemer, C. Nayak, M. Troyer, C.M. Marcus, C.J. Palmstrøm, Two-dimensional epitaxial superconductor-semiconductor heterostructures: A platform for topological superconducting networks, *Phys. Rev. B.* 93 (2016) 155402. <https://doi.org/10.1103/PhysRevB.93.155402>.
- [11] M. Kjaergaard, H.J. Suominen, M.P. Nowak, A.R. Akhmerov, J. Shabani, C.J. Palmstrøm, F. Nichele, C.M. Marcus, Transparent Semiconductor-Superconductor Interface and Induced Gap in an Epitaxial Heterostructure Josephson Junction, *Phys. Rev. Appl.* 7 (2017) 034029. <https://doi.org/10.1103/PhysRevApplied.7.034029>.

- 542 [12] W. Mayer, J. Yuan, K.S. Wickramasinghe, T. Nguyen, M.C. Dartiailh, J. Shabani,
543 Superconducting proximity effect in epitaxial Al-InAs heterostructures, *Appl. Phys. Lett.* 114
544 (2019). <https://doi.org/10.1063/1.5067363>.
- 545 [13] J.S. Lee, B. Shojaei, M. Pendharkar, A.P. McFadden, Y. Kim, H.J. Suominen, M.
546 Kjaergaard, F. Nichele, H. Zhang, C.M. Marcus, C.J. Palmstrøm, *Transport Studies of Epi-
547 Al/InAs Two-Dimensional Electron Gas Systems for Required Building-Blocks in
548 Topological Superconductor Networks*, *Nano Lett.* 19 (2019) 3083–3090.
549 <https://doi.org/10.1021/acs.nanolett.9b00494>.
- 550 [14] S. Guiducci, M. Carrega, G. Biasiol, L. Sorba, F. Beltram, S. Heun, *Toward Quantum Hall
551 Effect in a Josephson Junction*, *Phys. Status Solidi – Rapid Res. Lett.* 13 (2019) 1–5.
552 <https://doi.org/10.1002/pssr.201800222>.
- 553 [15] S. Guiducci, M. Carrega, F. Taddei, G. Biasiol, H. Courtois, F. Beltram, S. Heun, *Full
554 electrostatic control of quantum interference in an extended trenched Josephson junction*,
555 *Phys. Rev. B.* 99 (2019) 235419. <https://doi.org/10.1103/PhysRevB.99.235419>.
- 556 [16] F. Barati, J.P. Thompson, M.C. Dartiailh, K. Sardashti, W. Mayer, J. Yuan, K.
557 Wickramasinghe, K. Watanabe, T. Taniguchi, H. Churchill, J. Shabani, *Tuning Supercurrent
558 in Josephson Field-Effect Transistors Using h-BN Dielectric*, *Nano Lett.* 21 (2021) 1915–
559 1920. <https://doi.org/10.1021/acs.nanolett.0c03183>.
- 560 [17] B.H. Elfeky, N. Lotfizadeh, W.F. Schiela, W.M. Strickland, M. Dartiailh, K. Sardashti, M.
561 Hatefipour, P. Yu, N. Pankratova, H. Lee, V.E. Manucharyan, J. Shabani, *Local Control of
562 Supercurrent Density in Epitaxial Planar Josephson Junctions*, *Nano Lett.* 21 (2021) 8274–
563 8280. <https://doi.org/10.1021/acs.nanolett.1c02771>.
- 564 [18] F. Wen, J. Yuan, K.S. Wickramasinghe, W. Mayer, J. Shabani, E. Tutuc, *Epitaxial Al-InAs
565 Heterostructures as Platform for Josephson Junction Field-Effect Transistor Logic Devices*,
566 *IEEE Trans. Electron Devices.* 68 (2021) 1524–1529.
567 <https://doi.org/10.1109/TED.2021.3057790>.
- 568 [19] A. Hertel, L.O. Andersen, D.M.T. van Zanten, M. Eichinger, P. Scarlino, S. Yadav, J.
569 Karthik, S. Gronin, G.C. Gardner, M.J. Manfra, C.M. Marcus, K.D. Petersson, *Electrical
570 Properties of Selective-Area-Grown Superconductor-Semiconductor Hybrid Structures on
571 Silicon*, *Phys. Rev. Appl.* 16 (2021) 044015.
572 <https://doi.org/10.1103/PhysRevApplied.16.044015>.
- 573 [20] M. Sütő, T. Prok, P. Makk, M. Kirti, G. Biasiol, S. Csonka, E. Tóvári, *Near-surface InAs
574 two-dimensional electron gas on a GaAs substrate: Characterization and superconducting
575 proximity effect*, *Phys. Rev. B.* 106 (2022) 235404.
576 <https://doi.org/10.1103/PhysRevB.106.235404>.
- 577 [21] C. Ciaccia, R. Haller, A.C.C. Drachmann, T. Lindemann, M.J. Manfra, C. Schrade, C.
578 Schönenberger, *Gate-tunable Josephson diode in proximitized InAs supercurrent
579 interferometers*, *Phys. Rev. Res.* 5 (2023) 033131.
580 <https://doi.org/10.1103/PhysRevResearch.5.033131>.
- 581 [22] M. Coraiola, A.E. Svetogorov, D.Z. Haxell, D. Sabonis, M. Hinderling, S.C. ten Kate, E.
582 Cheah, F. Krizek, R. Schott, W. Wegscheider, J.C. Cuevas, W. Belzig, F. Nichele, *Flux-
583 Tunable Josephson Diode Effect in a Hybrid Four-Terminal Josephson Junction*, *ACS Nano.*
584 18 (2024) 9221–9231. <https://doi.org/10.1021/acsnano.4c01642>.
- 585 [23] S. Yan, H. Su, D. Pan, W. Li, Z. Lyu, M. Chen, X. Wu, L. Lu, J. Zhao, J.-Y. Wang, H. Xu,

- 586 Supercurrent, Multiple Andreev Reflections and Shapiro Steps in InAs Nanosheet Josephson
587 Junctions, *Nano Lett.* 23 (2023) 6497–6503. <https://doi.org/10.1021/acs.nanolett.3c01450>.
- 588 [24] Y.-J. Doh, J.A. van Dam, A.L. Roest, E.P.A.M. Bakkers, L.P. Kouwenhoven, S. De
589 Franceschi, Tunable Supercurrent Through Semiconductor Nanowires, *Science* (80-.). 309
590 (2005) 272–275. <https://doi.org/10.1126/science.1113523>.
- 591 [25] H.Y. Günel, I.E. Batov, H. Hardtdegen, K. Sladek, A. Winden, K. Weis, G. Panaitov, D.
592 Grützmacher, T. Schäpers, Supercurrent in Nb/InAs-nanowire/Nb Josephson junctions, *J.*
593 *Appl. Phys.* 112 (2012). <https://doi.org/10.1063/1.4745024>.
- 594 [26] P. Perla, H.A. Fonseka, P. Zellekens, R. Deacon, Y. Han, J. Kölzer, T. Mörstedt, B.
595 Bennemann, A. Espiari, K. Ishibashi, D. Grützmacher, A.M. Sanchez, M.I. Lepsa, T.
596 Schäpers, Fully in situ Nb/InAs-nanowire Josephson junctions by selective-area growth and
597 shadow evaporation, *Nanoscale Adv.* 3 (2021) 1413–1421.
598 <https://doi.org/10.1039/D0NA00999G>.
- 599 [27] A. Goswami, S.R. Mudi, C. Dempsey, P. Zhang, H. Wu, B. Zhang, W.J. Mitchell, J.S. Lee,
600 S.M. Frolov, C.J. Palmstrøm, Sn/InAs Josephson Junctions on Selective Area Grown
601 Nanowires with in Situ Shadowed Superconductor Evaporation, *Nano Lett.* 23 (2023) 7311–
602 7318. <https://doi.org/10.1021/acs.nanolett.3c01320>.
- 603 [28] N.W. Hendrickx, M.L. V. Tagliaferri, M. Kouwenhoven, R. Li, D.P. Franke, A. Sammak, A.
604 Brinkman, G. Scappucci, M. Veldhorst, Ballistic supercurrent discretization and micrometer-
605 long Josephson coupling in germanium, *Phys. Rev. B.* 99 (2019) 075435.
606 <https://doi.org/10.1103/PhysRevB.99.075435>.
- 607 [29] F. Vigneau, R. Mizokuchi, D.C. Zanuz, X. Huang, S. Tan, R. Maurand, S. Frolov, A.
608 Sammak, G. Scappucci, F. Lefloch, S. De Franceschi, Germanium Quantum-Well Josephson
609 Field-Effect Transistors and Interferometers, *Nano Lett.* 19 (2019) 1023–1027.
610 <https://doi.org/10.1021/acs.nanolett.8b04275>.
- 611 [30] K. Aggarwal, A. Hofmann, D. Jirovec, I. Prieto, A. Sammak, M. Botifoll, S. Martí-Sánchez,
612 M. Veldhorst, J. Arbiol, G. Scappucci, J. Danon, G. Katsaros, Enhancement of proximity-
613 induced superconductivity in a planar Ge hole gas, *Phys. Rev. Res.* 3 (2021) L022005.
614 <https://doi.org/10.1103/PhysRevResearch.3.L022005>.
- 615 [31] M. Zhu, M. Ben Shalom, A. Mishchenko, V. Fal’ko, K. Novoselov, A. Geim, Supercurrent
616 and multiple Andreev reflections in micrometer-long ballistic graphene Josephson junctions,
617 *Nanoscale.* 10 (2018) 3020–3025. <https://doi.org/10.1039/C7NR05904C>.
- 618 [32] T. Li, J.C. Gallop, L. Hao, E.J. Romans, Scalable, Tunable Josephson Junctions and DC
619 SQUIDs Based on CVD Graphene, *IEEE Trans. Appl. Supercond.* 29 (2019) 1–4.
620 <https://doi.org/10.1109/TASC.2019.2897999>.
- 621 [33] A.A. Generalov, K.L. Viisanen, J. Senior, B.R. Ferreira, J. Ma, M. Möttönen, M. Prunnila,
622 H. Bohuslavskyi, Wafer-scale CMOS-compatible graphene Josephson field-effect transistors,
623 *Appl. Phys. Lett.* 125 (2024). <https://doi.org/10.1063/5.0203515>.
- 624 [34] G. De Simoni, F. Paolucci, P. Solinas, E. Strambini, F. Giazotto, Metallic supercurrent field-
625 effect transistor, *Nat. Nanotechnol.* 13 (2018) 802–805. <https://doi.org/10.1038/s41565-018-0190-3>.
- 626
- 627 [35] G. De Simoni, C. Puglia, F. Giazotto, Niobium Dayem nano-bridge Josephson gate-
628 controlled transistors, *Appl. Phys. Lett.* 116 (2020). <https://doi.org/10.1063/5.0011304>.

- 629 [36] C. Puglia, G. De Simoni, N. Ligato, F. Giazotto, Vanadium gate-controlled Josephson half-
630 wave nanorectifier, *Appl. Phys. Lett.* 116 (2020). <https://doi.org/10.1063/5.0013512>.
- 631 [37] F. Capotondi, G. Biasiol, D. Ercolani, V. Grillo, E. Carlino, F. Romanato, L. Sorba, Strain
632 induced effects on the transport properties of metamorphic InAlAs/InGaAs quantum wells,
633 *Thin Solid Films.* 484 (2005) 400–407. <https://doi.org/10.1016/j.tsf.2005.02.013>.
- 634 [38] A. Paghi, G. Trupiano, G. De Simoni, O. Arif, L. Sorba, F. Giazotto, InAs on Insulator: A
635 New Platform for Cryogenic Hybrid Superconducting Electronics, (2024).
636 <http://arxiv.org/abs/2405.07630>.
- 637 [39] A. Paghi, S. Battisti, S. Tortorella, G. De Simoni, F. Giazotto, Cryogenic Behavior of High-
638 Permittivity Gate Dielectrics: The Impact of the Atomic Layer Deposition Temperature and
639 the Lithography Patterning Method, (2024). <http://arxiv.org/abs/2407.04501>.
- 640 [40] K.K. Likharev, Superconducting weak links, *Rev. Mod. Phys.* 51 (1979) 101–159.
641 <https://doi.org/10.1103/RevModPhys.51.101>.
- 642 [41] P. Dubos, H. Courtois, B. Pannetier, F.K. Wilhelm, A.D. Zaikin, G. Schön, Josephson critical
643 current in a long mesoscopic S-N-S junction, *Phys. Rev. B.* 63 (2001) 064502.
644 <https://doi.org/10.1103/PhysRevB.63.064502>.
- 645 [42] A. Iorio, A. Crippa, B. Turini, S. Salimian, M. Carrega, L. Chirolli, V. Zannier, L. Sorba, E.
646 Strambini, F. Giazotto, S. Heun, Half-integer Shapiro steps in highly transmissive InSb
647 nanoflag Josephson junctions, *Phys. Rev. Res.* 5 (2023) 033015.
648 <https://doi.org/10.1103/PhysRevResearch.5.033015>.

649

650